Nuclear excitation by electron capture in optical-laser-generated plasmas

Jonas Gunst,* Yuanbin Wu,† Christoph H. Keitel, and Adriana Pálffy‡
Max-Planck-Institut für Kernphysik, Saupfercheckweg 1, 69117 Heidelberg, Germany

(Received 29 March 2018; published 18 June 2018)

The process of nuclear excitation by electron capture in plasma environments generated by the interaction of ultrastrong optical lasers with solid-state samples is investigated theoretically. With the help of a plasma model, we perform a comprehensive study of the optimal parameters for the most efficient nuclear excitation and determine the corresponding laser setup requirements. We discern between the low-density plasma regime, modeled by scaling laws, and the high-density regime, for which we perform particle-in-cell calculations. As a nuclear transition case study we consider the 4.85-keV nuclear excitation starting from the long-lived ^{93m}Mo isomer. Our results show that the optimal plasma and laser parameters are sensitive to the chosen observable and that measurable rates of nuclear excitation and isomer depletion of ^{93m}Mo should be already achievable at laser facilities existing today.

DOI: 10.1103/PhysRevE.97.063205

I. INTRODUCTION

The invention of the laser more than 50 years ago [1] revolutionized atomic physics, leading to the better understanding and control of atomic and molecular dynamics. Covering several frequency scales, intense coherent light sources available today open unprecedented possibilities for the field of laser-matter interactions [2] also beyond atomic physics. Novel x-ray sources as the x-ray free-electron laser (XFEL) open, for instance, new possibilities to drive low-lying electromagnetic transitions in nuclei [3]. On the other hand, high-power optical lasers with their tremendous efficiency in transferring kinetic energy to charged particles may cause the formation of plasma [4], the host of complex interactions between photons, electrons, ions, and the atomic nucleus. Nuclear excitation in optical-laser-generated plasmas has been the general subject of several studies so far [5–18], while the possibilities to induce nuclear transitions to low-lying excited levels using high-energy lasers have been summarized in Refs. [19–23]. In addition, nuclear excitation mechanisms in cold high-density plasmas generated by the interaction of XFEL sources with solid-state targets were investigated in Refs. [24,25].

Nuclear excitation may occur in plasmas via several mechanisms. Apart from direct or secondary photoexcitation, the coupling to the atomic shell via processes such as nuclear excitation by electron capture (NEEC) or electron transition [26,27] may play an important role. In particular, it was shown that as a secondary process in the plasma environment, NEEC may exceed the direct nuclear photoexcitation at the XFEL by approximately six orders of magnitude [24,25]. Since the nuclear coupling to the atomic shell is, generally speaking, very sensitive to the plasma conditions, the question is raised whether one can tailor the latter for maximizing the effect of NEEC. While the tunability of the XFEL-generated plasma properties are limited due to the specific properties of x-ray–atom interaction, high-power optical lasers are able to generate plasmas over a broad parameter region as far as both temperature and plasma density are concerned. In a very recent Letter, NEEC was shown to be the dominant nuclear excitation mechanism for a broad parameter range in optical-laser-generated plasmas, and results on tailored optical-laser parameters for maximizing NEEC were presented [28].

In this work, we present a systematic theoretical study of NEEC in optical-laser-generated plasmas. Having the concrete scenario of ultrashort optical-laser-generated plasmas in mind, we develop a plasma model that can be easily applied to any nuclear parameters. Based on this model, we deduce the optimal NEEC parameters in terms of plasma temperature and density. Due to the complexity of the processes involved, we show that the plasma parameters for the maximal NEEC rate are not identical to the ones that determine the maximal number of excited nuclei. We then further investigate how the optimal NEEC parameters in the temperature-density landscape can be accessed by a short and intense laser pulse considering various experimental conditions such as laser intensity, wavelength, pulse duration, or pulse energy. We discern in our treatment between two cases, the low-density plasma regime, modeled by the scaling law, and the high-density regime, where we use dedicated particle-in-cell (PIC) simulations.

As a case study we consider the 4.85-keV nuclear transition starting from a long-lived excited state of ^{93}Mo at 2.4 MeV. Such states are also known as nuclear isomers [29] and have been the subject of increased attention due to the potential storage of large amounts of energy over long periods of time [30–36]. For ^{93m}Mo, the additional 4.85-keV nuclear excitation leads to the depletion of the isomer and release on demand of the stored energy. Apart from this appealing scenario, ^{93m}Mo is interesting also because of the recently reported observation of isomer depletion via NEEC of the 4.85-keV transition [37]. Our results show that for high electron densities, NEEC is actually the dominant nuclear excitation channel for ^{93m}Mo,

*jonas.gunst@mpi-hd.mpg.de
†yuanbin.wu@mpi-hd.mpg.de
‡palffy@mpi-hd.mpg.de

surpassing by orders of magnitude photoexcitation in the plasma. Surprisingly, a six-order-of-magnitude increase in the number of excited nuclei can be achieved by employing a high-power optical laser compared to the previously investigated case of XFEL-generated plasmas. The calculated maximal number of depleted isomers for realistic laser setup parameters appears to have reached values large enough to be observable in an experiment. Although still far from the final goal, this is a further milestone on the way to the realization of controlled energy storage and release via nuclear isomers.

This paper is structured as follows. After introducing the theory for NEEC and nuclear photoexcitation in a plasma environment and the employed plasma model in Sec. II, we start by investigating the optimal plasma conditions for NEEC in terms of electron density and temperature based on a simplified model for spherical plasmas in Sec. III. As part of this section we discuss the influence of ionization potential depression, the expected contribution from photoexcitation, and a hydrodynamic model for plasma expansion. Section IV is then devoted to optical-laser-generated plasmas. Since the plasma generation involves different processes depending on the electron density, we divide this section into two parts, Sec. IV A for low-density plasmas and Sec. IV B for high-density plasmas. As a main result we evaluate the optimal laser parameters for low-density scenarios at the example of high-power laser facilities. Surprisingly, our analysis of a PIC simulation for high electron densities shows that similar nuclear excitation numbers can be achieved with 100-J lasers available at many facilities around the world. Section V summarizes our conclusions.

II. THEORETICAL APPROACH

This section introduces the theoretical approach used for describing nuclear excitation in the plasma. After general considerations on the setup, we will sketch our calculations for NEEC and photoexcitation rates in the plasma and outline the used plasma model. Atomic units $\hbar = m_e = e = 4\pi\varepsilon_0 = 1$ are used throughout Secs. II B and II C.

A. General considerations

We investigate the interaction of ultrastrong lasers with a solid-state target. The strong electromagnetic field of optical lasers leads to field ionization and acceleration of the electrons in the target. The accelerated hot electrons can lead to further ionization of the target via collisional ionization. Since the laser wavelength is in the optical range, the electronic heating occurs essentially at the surface of the material. The hot electrons produced by the laser are accelerated away from the interaction region generating an electric field due to the charge separation. Attracted by this electric field, the ions subsequently follow the hot electrons, resulting in the formation of a neutral plasma surrounding the target. The timescale of the plasma generation process is on the order of the pulse duration (plus the time for the acceleration of the ions). Moreover, near the focal spot of the laser, the plasma can be considered as uniform in terms of electron density and temperature.

Looking in more detail at the start of the laser-target interaction, there will be a prepulse leading to the generation of a preplasma. The main pulse thus interacts with this cold preplasma instead of the initial target. Consequently, the final plasma consists of a cold (coming from the prepulse) and a hot electron distribution (coming from the main pulse). The cold electron distribution stays essentially in the region around the interaction point with the target. Insofar as we consider thin targets (on the order of microns), this volume is small in comparison to the total plasma volume such that the cold electrons can be neglected.

In order to reach high electron densities ($\sim 10^{22}$ cm^{-3}), thicker targets need to be considered. Analogously to the case of thin targets, the electromagnetic laser field accelerates the electrons of the target surface into the inner region of the target. These hot electrons then subsequently lead to further collisional ionization events inside the target which can result in a very dense plasma in this region [38,39]. However, the absorption fraction f seems to be effectively much lower for this heating mechanism in comparison to the thin target case.

For our particular study of nuclear excitation in plasmas, we consider a strong optical laser that interacts with a solid-state target containing a fraction of nuclei in the isomeric state. Nuclear excitation by electron capture and/or photoexcitation may occur in the generated plasma. In the resonant process of NEEC, a free electron recombines into a vacant bound atomic state with the simultaneous excitation of the nucleus. The isomers can then be excited to a trigger state which rapidly decays to the nuclear ground state and releases the energy "stored" in the isomer. For ^{93m}Mo the stored energy corresponds to the isomeric state at 2424 keV. A further 4.85-keV excitation leads to the fast release within approximately 4 ns via a decay cascade containing a 1478-keV photon which could serve as a signature of the isomer depletion. Recent experimental results on the isomer depletion of ^{93m}Mo in a channeling setup have deduced a rather high NEEC rate of the 4.85-keV transition [37], encouraging further studies of this nuclear transition.

B. The NEEC in plasma environments

In the plasma, free electrons with different kinetic energies are available. At the NEEC resonant energy, electrons may recombine into ions, leading to nuclear excitation. The resonance bandwidth is determined by a narrow Lorentz profile. Since the kinetic energy of free electrons in a plasma is distributed over a wide range, many resonant NEEC channels may exist. In the following we will shortly describe how such a situation can be handled theoretically in terms of reaction rates.

In order to restrict the number of possible initial electron configurations, for a lower-limit estimate, we consider in the following only NEEC into ions which are in their electronic ground states. In this case, the initial electronic configuration α_0 is uniquely identified by the charge state number q before electron capture. In the isolated resonance approximation, the total NEEC reaction rate in the plasma can be written as a summation over all charge states q and all capture channels α_d,

$$\lambda_{\mathrm{NEEC}}(T_e,n_e) = \sum_q \sum_{\alpha_d} P_q(T_e,n_e)\lambda_{\mathrm{NEEC}}^{q,\alpha_d}(T_e,n_e). \quad (1)$$

Here P_q is the probability to find in the plasma ions in the charge state q as a function of electron temperature T_e and density n_e. The partial NEEC rate into the capture level α_d of an ion in the charge state q can be expressed by the convolution over the electron energy E of the single-resonance NEEC cross section $\sigma_{\mathrm{NEEC}}^{i\to d}$ and the free-electron flux ϕ_e,

$$\lambda_{\mathrm{NEEC}}^{q,\alpha_d}(T_e,n_e) = \int dE\, \sigma_{\mathrm{NEEC}}^{i\to d}(E)\phi_e(E,T_e,n_e). \tag{2}$$

The NEEC cross section $\sigma_{\mathrm{NEEC}}^{i\to d}$ as a function of the free-electron energy E is proportional to a Lorentz profile $L_d(E - E_d)$ centered on the resonance energy E_d. The width of the resonance is typically determined by the nuclear linewidth of approximately 100 neV. Since over this energy scale ϕ_e can safely be considered as constant, we can approximate the Lorentz profile by a Dirac δ-like function. The match between the resonance energy E_d and the functional temperature dependence of the electron flux $\phi_e(T_e)$ determines the quantitative contribution of the individual NEEC channels.

The electron flux ϕ_e in the plasma can be written as the product of the density of states $g_e(E)$, the Fermi-Dirac distribution $f_{\mathrm{FD}}(E,T_e,n_e)$ for a certain electron temperature T_e, and the velocity $v(E)$,

$$\phi_e(E,T_e,n_e)dE = g_e(E) f_{\mathrm{FD}}(E,T_e,n_e)v(E)dE. \tag{3}$$

The temperature dependence of ϕ_e is only included in the Fermi-Dirac statistics f_{FD} [40]. The density of states and the velocity are determined by considering the relativistic dispersion relation for the free electrons. The electronic chemical potential μ_e occurring in the expression of f_{FD} is fixed by adopting the normalization

$$\int dE\, g_e(E) f_{\mathrm{FD}}(E,T_e,n_e) = n_e. \tag{4}$$

Thus, the electron flux in the plasma depends on both the electron temperature T_e and the density n_e.

The theoretical formalism for the calculation of the NEEC cross section σ_{NEEC} has been presented elsewhere [24,25,41,42]. The cross section is connected to the microscopic NEEC reaction rate Y_{NEEC} via

$$\sigma_{\mathrm{NEEC}}^{i\to d}(E) = \frac{2\pi^2}{p^2} Y_{\mathrm{NEEC}}^{i\to d} L_d(E - E_d), \tag{5}$$

with p the free-electron momentum. Substituting Eq. (5) into Eq. (2), the integral over the kinetic electron energy E can be solved by assuming that the free-electron momentum p and the NEEC rate Y_{NEEC} are constant over the width of the Lorentz profile $L_d(E - E_d)$, which is the case for a wide spectrum of isotopes. Equation (2) then simplifies to

$$\lambda_{\mathrm{NEEC}}^{q,\alpha_d}(T_e,n_e) = \frac{2\pi^2}{p^2} Y_{\mathrm{NEEC}}^{i\to d}\phi_e(E_d,T_e,n_e). \tag{6}$$

The total NEEC rate λ_{NEEC} in Eq. (1) is therefore strongly dependent on the available charge states and free-electron energies which both are dictated by the plasma conditions. Taking the spatial and temporal plasma evolution into account, the total NEEC number N_{exc} is connected to the rate λ_{NEEC} via

$$N_{\mathrm{exc}} = \int_{V_p} d^3\mathbf{r} \int dt\, n_{\mathrm{iso}}(\mathbf{r},t)\lambda_{\mathrm{NEEC}}(T_e,n_e;\mathbf{r},t), \tag{7}$$

where n_{iso} denotes the number density of isomers present in the plasma. For a further quantitative estimate of the occurring nuclear excitation, relevant factors are the interaction time and the volume over which the interaction takes place, considered to be the plasma volume V_p. These aspects are detailed in Sec. II D.

C. Resonant nuclear photoexcitation in plasma

Instead of undergoing NEEC, the nucleus can also be excited by the absorption of a photon which has to be on resonance with the nuclear transition energy E_n. Analogously to Eqs. (1) and (2), the excitation rate via photons in the plasma can be expressed as

$$\lambda_\gamma(T_e,n_e) = \int \sigma_\gamma^{i\to d}(E)\phi_\gamma(E,T_e,n_e)dE, \tag{8}$$

with the nuclear photoexcitation cross section $\sigma_\gamma^{i\to d}(E) = \frac{2\pi^2}{k^2} A_\gamma^{i\to d} L_d(E - E_n)$, where $A_\gamma^{i\to d}$ represents the corresponding rate. For the calculation of the photoexcitation rate, we have adopted the formalism from Ref. [43] that connects A_γ with so-called reduced nuclear transition probabilities. For the latter we employ experimental data and/or nuclear model calculations later on.

In general, the photon flux and hence the photoexcitation rate in the plasma depend on the prevailing plasma conditions represented by electron temperature and density in Eq. (8). In order to evaluate this dependence further, we employ two models for the photon flux ϕ_γ in the following.

First, we assume the photons to be in thermodynamic equilibrium (TDE) with the electrons such that a blackbody distribution is applicable, resulting in the density-independent photon flux

$$\phi_\gamma^{\mathrm{TDE}}(E,T_e)dE = c g_\gamma(E) f_{\mathrm{BE}}(E,T_e)dE. \tag{9}$$

Here c is the speed of light, g_γ represents the photonic density of states, and f_{BE} denotes the Bose-Einstein distribution [40]. Substituting Eq. (9) into Eq. (8) leads to the photoexcitation rate under TDE conditions

$$\lambda_\gamma^{\mathrm{TDE}}(T_e) = \frac{2\pi^2}{k^2} A_\gamma^{i\to d}\phi_\gamma^{\mathrm{TDE}}(E_n,T_e). \tag{10}$$

In the derivation of Eq. (10), the Lorentzian profile has been approximated by a Dirac δ-like resonance since the nuclear transition width is, for the considered plasma temperatures, much smaller than the energy region over which the photon flux varies significantly.

As a second model we consider the process of bremsstrahlung as a potential photon source in the plasma. According to Ref. [5], the photon flux emitted via bremsstrahlung evaluates to

$$\phi_\gamma^B(E,E_e,T_e,n_e)dE dE_e = t_i\left(\frac{d\sigma_B(E_e)}{dE}\right)\phi_e(E_e,T_e,n_e)dE dE_e, \tag{11}$$

where $d\sigma_B(E_e)/dE$ denotes the bremsstrahlung cross-section differential in the emitted photon energy E and t_i represents the target thickness given in atoms per area. For the calculations later on we consider $t_i = n_i R_p$, where n_i represents the ion

number density in the plasma and R_p the plasma radius. Employing Eq. (11), the photoexcitation rate in the plasma with photons emitted via bremsstrahlung is given by

$$\lambda_\gamma^B(T_e,n_e) = \frac{2\pi^2}{k^2} A_\gamma^{i\to d} \int \phi_\gamma^B(E_n,E_e,T_e,n_e) dE_e, \quad (12)$$

where the same approximation as for the blackbody spectrum has been used to solve the integration over the kinetic electron energy E. The photon flux on resonance occurring in Eq. (12) is determined by

$$\phi_\gamma^B(E_n,E_e,T_e,n_e) = \left(\frac{d\sigma_B(E_e)}{dE}\right)_{E=E_n} \phi_e(E_e,T_e,n_e). \quad (13)$$

Replacing λ_{NEEC} by the corresponding photoexcitation rate [Eq. (10) or (12)] in Eq. (7), the total number of excited nuclei via resonant nuclear photoexcitation can be evaluated. A comparison of the NEEC and resonant photon absorption rates in the plasma is presented in Sec. III C for a variety of plasma conditions.

D. Plasma model

For the plasma modeling part here and in the following, SI units with $k_B = 1$ are adopted, unless for some quantities the units are explicitly given.

1. General model for spherical plasmas

In order to get a general idea of the number of excited nuclei in the plasma, we first disregard the exact target heating processes and assume in a first approximation a spherical plasma with homogeneous electron temperature T_e and density n_e over the plasma lifetime τ_p. With that the total number of excited nuclei determined in Eq. (7) evaluates to

$$N_{\mathrm{exc}} = N_{\mathrm{iso}} \lambda_{\mathrm{NEEC}}(T_e,n_e)\tau_p, \quad (14)$$

with N_{iso} being the number of isomers in the plasma. Here N_{iso} can be estimated by introducing the isomer fraction embedded in the original solid-state target f_{iso},

$$N_{\mathrm{iso}} = f_{\mathrm{iso}} n_i V_p, \quad (15)$$

where n_i stands for the ion number density in the plasma and the plasma volume V_p is given by $V_p = \frac{4}{3}\pi R_p^3$ with the plasma radius R_p. In neutral plasmas, the ion and electron densities are related via the average charge state $\bar{Z}$,

$$n_i = n_e/\bar{Z}. \quad (16)$$

In the case of ^{93m}Mo isomer triggering, an isomer fraction of $f_{\mathrm{iso}} \approx 10^{-5}$ embedded in solid-state niobium foils can be generated by intense ($\geqslant 10^{14}$ protons/s) beams [24] via the $^{93}_{41}\mathrm{Nb}(p,n)^{93m}_{42}\mathrm{Mo}$ reaction [44].

Moreover, the plasma lifetime τ_p occurring in Eq. (14) can be approximated for spherical plasmas by following an estimate for spherical clusters [45]. The timescale after which the plasma's spatial dimension is approximatively doubled is given as a function of plasma radius, electron temperature, and average charge state by

$$\tau_p = R_p\sqrt{m_i/(T_e\bar{Z})}, \quad (17)$$

with the ion mass m_i. Note that τ_p is implicitly also influenced by the electron density n_e due to the dependence $\bar{Z}(T_e,n_e)$.

Based on the expression of the plasma lifetime τ_p in Eq. (17), the total number of excited nuclei in the plasma can be estimated. This approximative approach is easily applicable to other nuclear transitions and provides many instructive insights into plasma-mediated nuclear excitations as shown later on in considering the example of ^{93m}Mo triggering. In order to test the validity of the plasma lifetime approach, we perform a comparison with results from a hydrodynamic model for the plasma expansion.

2. Hydrodynamic expansion

Following the analysis in Ref. [25], we consider a more detailed hydrodynamic model for the plasma expansion by a quasineutral expansion of spherical clusters as studied in the context of the intense optical-laser pulse interaction with spherical clusters [45,46]. During the expansion, the plasma is assumed to maintain a uniform (but decreasing) density throughout the plasma sphere while the electron temperature decreases with the adiabatic expansion of the plasma,

$$\tfrac{3}{2} n_{e,t} V dT_{e,t} = -P_e dV, \quad (18)$$

where $n_{e,t}$ is the number density of free electrons, $V = 4\pi R_t^3/3$ is the volume of the plasma with the radius R_t, and $P_e = n_{e,t}T_{e,t}$ is the pressure of free electrons. The time-dependent electron temperature and the plasma radius satisfy the relation

$$T_{e,t} = T_e\left(\frac{R_p}{R_t}\right)^2, \quad (19)$$

where T_e is the initial electron temperature and R_p the initial plasma radius. During the plasma expansion, the electrons lose their thermal energy to the ions, resulting in the electron and ion kinetic energies

$$n_{i,t}\frac{dT_{i,t}}{dt} = -n_{e,t}\frac{dT_{e,t}}{dt}, \quad (20)$$

$$\frac{1}{2}m_i\left(\frac{dR_t}{dt}\right)^2 = \frac{3}{2}T_{i,t}, \quad (21)$$

where $n_{i,t}$ is the ion number density, $T_{i,t}$ is the ion temperature, and m_i is the ion mass. The electron and ion collisions take place on a much shorter timescale than the plasma expansion time such that we can consider the temperature to be uniform throughout the sphere [45]. The equation of plasma expansion is given by

$$m_i\frac{d^2R_t}{dt^2} = 3Z\frac{T_e R_p^2}{R_t^3}, \quad (22)$$

where Z is the ratio of the electron density to the ion density, i.e., the average charge state of the ions in the quasineutral limit. Solving Eq. (22) for a fixed $Z = \bar{Z}$ under the condition that the initial speed for cluster expansion is zero, one obtains the plasma lifetime expression τ_p in Eq. (17) as the expansion time for increasing the plasma radius by a factor 2.

Rate estimates based on the FLYCHK code [47,48] show that the timescale to reach the steady state varies from the order of 10 fs for solid-state density to the order of 10 ps for low

density $\sim 10^{19}$ cm^{-3} at temperature ~ 1 keV (for the plasma constituents under consideration in the present work). For solid-state density plasmas, 10 fs is much shorter than the time interval that we are analyzing for NEEC in this work. For the low-density case, 10 ps is normally longer than the laser pulse duration. However, the relevant timescale to compare with is not the pulse duration, but rather the lifetime of the plasma, over which NEEC takes place. As discussed below, such low-density plasmas generated by the laser-target interaction under consideration last a few hundred picoseconds. Therefore, we can conclude that the timescale for reaching the steady state (with regard to the atomic processes) is much smaller than the expansion timescale for the plasmas conditions under consideration here. We thus may assume that the steady state with regard to the atomic processes is established at each time instant during the expansion.

3. *Laser-induced plasma: Scaling law*

Considering the case of a low-density (underdense) plasma, which can be generated via the interaction of a strong optical laser with a thin target, the plasma-generation process typically evolves in two steps [49]: (i) a preplasma is formed by the prepulse of the laser and (ii) this preplasma is subsequently heated by the main laser pulse potentially up to keV electron energies. We model the plasma following the approach in Refs. [49,50]. With the help of a so-called scaling law, the plasma conditions can be mapped to laser parameters, such as laser intensity $I_{\rm laser}$, wavelength $\lambda_{\rm laser}$, pulse duration $\tau_{\rm laser}$, and pulse energy $E_{\rm pulse}$. Assuming a flat-top beam profile and for a fixed focal radius $R_{\rm focal}$ the laser intensity reads

$$I_{\rm laser} = \frac{E_{\rm laser}}{\tau_{\rm laser} \pi R_{\rm focal}^2}. \tag{23}$$

We adopt here at first the widely used ponderomotive scaling law in the nonrelativistic limit (sharp-edged profiles)

$$T_e \approx 3.6 I_{16} \lambda_\mu^2 \text{ keV}, \tag{24}$$

where I_{16} is the laser intensity in units of 10^{16} W/cm^2 and λ_μ the wavelength in microns [51–53].

Depending on the target and laser-target interaction conditions, different electron temperature scalings are used in the literature [53]. For comparison, we adopt here also a second scaling law (known as the short-scale length profile) [53,54]

$$T_e \approx 8\left(I_{16}\lambda_\mu^2\right)^{1/3} \text{ keV}. \tag{25}$$

The electron density can be estimated as $n_e = N_e/V_p$, where N_e is the total number of electrons which can be related to the absorbed laser energy $f E_{\rm pulse}$ via

$$N_e = \frac{f E_{\rm pulse}}{T_e}. \tag{26}$$

The absorption coefficient f saturates at around 10%–15% for high irradiances and steep density profiles [53]. However, in the case of moderate intensities and intermediate scale lengths (e.g., $I\lambda^2 = 10^{16}$W cm^{-2} μm^2 and $L/\lambda \sim 0.1$), the absorption can be much higher, with f taking values up to 70% [53].

The plasma volume in the case of a laser-generated plasma is given by

$$V_p = \pi R_{\rm focal}^2 d_p, \tag{27}$$

where the plasma thickness $d_p = c\tau_{\rm pulse}$ is determined by the laser pulse duration $\tau_{\rm pulse}$. In contrast to the pure spherical plasma, we consider here a cylindrical geometry with the transversal length dimension determined by the focal radius of the laser $R_{\rm focal}$ and the longitudinal length scale via the plasma thickness d_p.

Nevertheless, for the case of focal radius, plasma thickness, and plasma radius of similar scale, we may again consider the plasma lifetime given by Eq. (17) derived for the spherical plasma model. For a lower-limit estimate of the nuclear excitation, we use the smallest length scale out of $R_{\rm focal}$ and d_p to calculate τ_p,

$$\tau_p = \begin{cases} R_{\rm focal}\sqrt{m_i/(T_e\bar{Z})} & \text{for } R_{\rm focal} < d_p \\ d_p\sqrt{m_i/(T_e\bar{Z})} & \text{for } d_p \leqslant R_{\rm focal}. \end{cases} \tag{28}$$

III. NUMERICAL RESULTS FOR SPHERICAL PLASMAS

A. The NEEC results

The net NEEC rate $\lambda_{\rm NEEC}$ is a function of the prevailing plasma conditions, e.g., electron temperature T_e and density n_e. As presented in the preceding section, our model essentially consists of two separate parts which are combined to calculate the NEEC rate in the plasma: (i) the microscopic NEEC cross sections and (ii) the macroscopic plasma conditions such as charge state distribution and electron flux.

The microscopic NEEC cross sections are calculated by employing bound atomic wave functions from a multiconfigurational Dirac-Fock method implemented in the GRASP92 package [55] and solutions of the Dirac equation with $Z_{\rm eff} = q$ for the continuum. For both types of wave functions, we do not consider the effects of the plasma temperature and density, which are sufficiently small to be neglected in the final result of the nuclear excitation. The occurring nuclear matrix elements can be related to the reduced transition probability $B(E2)$ for which the calculated value of 3.5 W.u. (Weisskopf units) [56] was used.

Numerical results for the individual NEEC cross sections of all considered capture channels are presented as a function of the kinetic electron energy in Fig. 1. We recall that the capture energy needs to coincide with the nuclear transition energy E_n, e.g., 4.85 keV in the case of ^{93m}Mo triggering. Therefore, each peak represents a Lorentzian resonance located at $E_{\rm res} = E_n - E_{\alpha_d}$, where E_{α_d} stands for the atomic binding energy of the considered capture channel α_d. The width of the Lorentzian profile is given by the natural width of the nuclear triggering state T which is composed of the radiative decay and internal conversion channels leading to approximately 130 neV.

Figure 1 shows that NEEC prefers the capture into deeply bound states as the cross-section peak values increase for decreasing resonance energy of the free electrons. The resonance window for L-shell capture lies between 52 and 597 eV, for the M shell between 2118 and 4308 eV, for the N shell between 3320 and 4677 eV, and for the O shell between 3874 and 4743 eV, as illustrated by the horizontal lines in

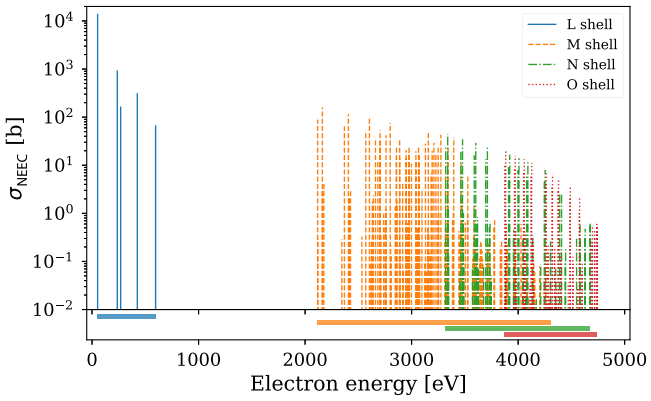

FIG. 1. Microscopic NEEC cross sections as a function of the kinetic electron energy. The considered resonance channels for capture into the L shell (blue solid line), M shell (orange dashed line), N shell (green dash-dotted line), and O shell (red dotted) are shown together with the corresponding resonance energy windows (horizontal bars just above the x axis).

Fig. 1. Hence, there is a gap between approximately 600 and 2100 eV without any NEEC resonance channels. Note that NEEC into the K shell is energetically forbidden for the 4.85-keV transition in ^{93}Mo.

The capture into the $2p_{3/2}$ orbital for ions with initial charge state $q = 36$ and an initial electron configuration of $1s^2 2s^2 2p_{1/2}^2$ leads to the highest NEEC resonance strength (integrated cross section) of 2.78×10^{-3} b eV. The corresponding resonance energy is at an electron energy of 52 eV. Interestingly, for higher charge states NEEC into the L shell is energetically forbidden because the binding energies exceed the nuclear transition energy of 4.85 keV.

For the calculation of the net NEEC rate in the plasma, the microscopic NEEC cross sections have to be combined with the macroscopic plasma parameters according to Eqs. (1) and (2). We model the plasma conditions by a relativistic distribution for the free electrons and the converged charge state distribution computed with the radiative-collisional code FLYCHK [48] assuming the plasma to be in its nonlocal thermodynamical equilibrium steady state. The population kinetics model implemented in FLYCHK is based on rate equations including radiative and collisional processes, Auger decay, and electron capture. These rate equations are solved for a finite set of atomic levels which consists of ground states, single excited states ($n \leqslant 10$), autoionizing doubly excited states, and inner-shell excited states for all possible ionic stages. Employing a schematic atomic structure, the atomic energy levels are computed from ionization potentials where the effect of ionization potential depression occurring in plasmas is taken into account by the model of Stewart and Pyatt [57].

While the charge state distribution is described as a function of plasma parameters $P_q(T_e, n_e)$, a simplified model is used for the atomic orbital population. For a specific charge state q, we assume (not necessarily to our advantage) that the charged ion is in its ground state initially (before NEEC) and capture of an additional electron occurs in a free orbital.

Numerical results for λ_{NEEC} and the total number of excited isomers N_{exc} are presented in Fig. 2 in parallel with the corresponding electron fluxes and charge state distributions. The calculation of the net NEEC rate involves charge states from $q = 14$ up to the bare nucleus ($q = 42$) with 333 NEEC capture states in total, composed of 5 L-shell, 168 M-shell, 70 N-shell, and 90 O-shell orbitals. The results for the dominant recombination channels into the L and M atomic shells are presented individually in Fig. 2. For the total NEEC rate λ_{NEEC}, further smaller contributions from the recombination into the N and O shells were also taken into account. For the computation of N_{exc}, an arbitrary plasma radius of 40 μm has been assumed.

Both λ_{NEEC} and N_{exc} increase with increasing electron density n_e. In the range $n_e = 10^{19}$–10^{20} cm^{-3}, our calculations show that the charge state distribution P_q is nearly unaffected for high temperatures T_e. In the same time, λ_{NEEC} is enhanced by a factor of 10, maintaining almost the same functional dependence on electron temperature. This indicates that at low densities the boost in λ_{NEEC} is (almost) a pure density effect coming from the increasing number of free electrons present in the plasma ($\phi_e \propto n_e$). Increasing the electron density to even higher values, the behavior of λ_{NEEC} and N_{exc} becomes more involved as the charge distribution P_q shows a complex dependence on the plasma conditions n_e and T_e. Between $n_e = 10^{21}$ and 10^{24} cm^{-3} we see that with increasing n_e the atomic shell contributions change significantly and λ_{NEEC} is substantially enhanced.

Apart from the available charge states in the plasma, the match between the electron distribution [Fig. 2(a)] and the NEEC resonance conditions (Fig. 1) plays an important role in this behavior. The electron distributions reach their maxima at an energy $E \sim T_e$. For energies below this value (e.g., where the resonance energies for captures into the L shell are located) more electrons are available for lower temperatures. In contrast, the high-energy tail of the electron distribution drops exponentially with e^{-E/T_e} and is therefore faster decreasing the lower the temperature. In the case of ^{93m}Mo triggering and temperatures in the keV range, the energy region $E \gtrsim T_e$ is in particular important for NEEC into the higher shells M, N, and O.

As seen from Fig. 1, the best case for NEEC would be to have the maximum of the electron distribution ($E \sim T_e$) located at the resonance channels with the highest cross sections (e.g., capture into the L shell). However, assuming that the ions are always in their ground states initially, this condition cannot be exactly fulfilled, because lower temperatures also lead to lower charge states present in the plasma such that the L-shell capture will be closed. The corresponding electron energy window and charge state range for the L-shell resonances are highlighted by the gray-shaded areas in Fig. 2.

These contradicting requirements for efficient NEEC suggest that there is a temperature T_{max} at which the plasma-mediated NEEC triggering reaches a maximum for each density value n_e. The temperatures T_{max} for N_{exc} and for the total and partial shell contributions λ_{NEEC} are depicted as a function of the electron density in Figs. 2(c) and 2(d). Naively, one would expect that T_{max} is approximately the same for N_{exc} and for λ_{NEEC}. This is however only true at high densities starting from 10^{21} cm^{-3}. According to our approximation in Eq. (17), the chosen plasma lifetime is T_e dependent. In particular, at low electron densities τ_p acts as a weighting function proportional to $(T_e)^{-1/2}$, shifting the maximum of N_{exc} to lower temperatures. The optimal plasma conditions for the total excitation number can thus drastically differ from

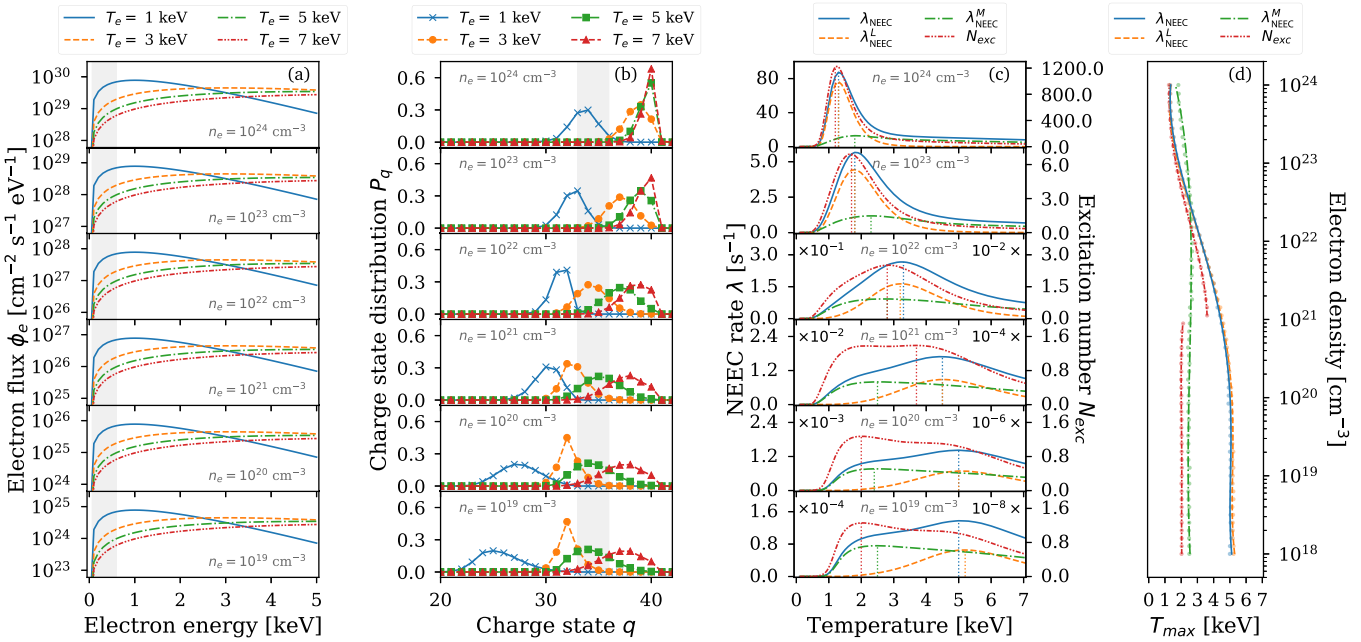

FIG. 2. (a) Electron flux ϕ_e and (b) charge state distributions (calculated with the help of FLYCHK) shown for temperatures $T_e = 1$ keV (blue solid curve for ϕ_e and blue solid curve with crosses for the charge state distribution), 3 keV (orange dashed curve for ϕ_e and orange dashed curve with closed circles for the charge state distribution), 5 keV (green dash-dotted curve for ϕ_e and green dash-dotted curve with closed squares for the charge state distribution), and 7 keV (red dash–double-dotted curve for ϕ_e and red dashed curve with closed triangles for the charge state distribution) at selected electron densities ranging from 10^{19} up to 10^{24} cm^{-3}. Electron energy and charge state ranges for L-shell capture are shaded in gray. (c) The NEEC rate λ_{NEEC} (blue solid curve) and the total number of excited isomers N_{exc} (red dash-dot-dotted curve), as well as the individual contributions $\lambda^L_{\mathrm{NEEC}}$ (orange dashed curve) and $\lambda^M_{\mathrm{NEEC}}$ (green dash-dotted curve) from the L and M shells, respectively, shown as a function of the electron temperature T_e for the selected electron densities n_e. A plasma radius of 40 μm has been assumed in the calculations of N_{exc}. (d) Temperatures T_{max} as a function of density, for maximizing N_{exc}, λ_{NEEC}, $\lambda^L_{\mathrm{NEEC}}$ and $\lambda^M_{\mathrm{NEEC}}$, respectively, at each particular n_e.

the optimal conditions for λ_{NEEC} in this model. We note that the arbitrary choice of R_p only influences the absolute scale of the NEEC number, not the position of T_{max}.

B. Ionization potential depression

While the effect of plasma-induced ionization potential depression (IPD) is taken into account for the charge state distribution (included in FLYCHK), it is neglected in the calculation of the microscopic NEEC cross sections and hence in the NEEC resonance energies so far. In order to quantify the effect of the variation of atomic orbital energy on our final results, we adopted the model of Stewart and Pyatt [57] under the following assumptions: (i) The bound electronic wave functions are unchanged, (ii) the binding energies of atomic orbitals are lowered due the ionization potential depression $\Delta V(q,T_e,n_e)$, (iii) the free-electron wave functions are computed with $Z_{\mathrm{eff}} = q$, and (iv) the kinetic energy of the electrons required to match the NEEC resonance condition for a given orbital is modified according to the reduction of the corresponding binding energy. Note that due to our approach for the potential lowering there might appear additional NEEC capture channels at low resonance energies (e.g., L-shell orbitals), while resonances disappear at resonance energies close to the nuclear transition energy.

The IPD given by the model of Stewart and Pyatt [57] is (using Gaussian units with $k_B = 1$)

$$\Delta V = \frac{ze^2}{\lambda_D} \tag{29}$$

for the weak-coupling limit, i.e., $(a/\lambda_D)^3 \ll 1$, and

$$\Delta V = \frac{3}{2}\frac{ze^2}{a} \tag{30}$$

for the strong-coupling limit, i.e., $(a/\lambda_D)^3 \gg 1$. Here λ_D is the Debye length,

$$\frac{1}{\lambda_D^2} = \frac{4\pi e^2}{T}(z^* + 1)n_e, \tag{31}$$

and a is the ion-sphere radius for an ion of net charge z defined by

$$4\pi a^3/3 = z/n_e. \tag{32}$$

The net charge z is the charge state of the concerned ion (central ion) after the ionization, i.e., the above IPD expressions (29)–(32) describe the process of removing an electron from an ion with charge $(z-1)^+$. Furthermore, $z^* = \langle z^2\rangle/\langle z\rangle$, $\langle z\rangle$ is the averaged charge state of the plasma, and $\langle z^2\rangle$ is the average of the charge state square of the plasma.

The ionization potential lowering may change the binding energies from a few eV to hundreds of eV depending on the considered charge state q and the prevailing plasma conditions in terms of T_e and n_e. In Fig. 3 the relative change in the net NEEC rate due to IPD defined as

$$\Delta_{\mathrm{IPD}}(T_e,n_e) = \frac{\lambda_{\mathrm{NEEC}}(T_e,n_e) - \lambda^{\mathrm{IPD}}_{\mathrm{NEEC}}(T_e,n_e)}{\lambda_{\mathrm{NEEC}}(T_e,n_e)} \tag{33}$$

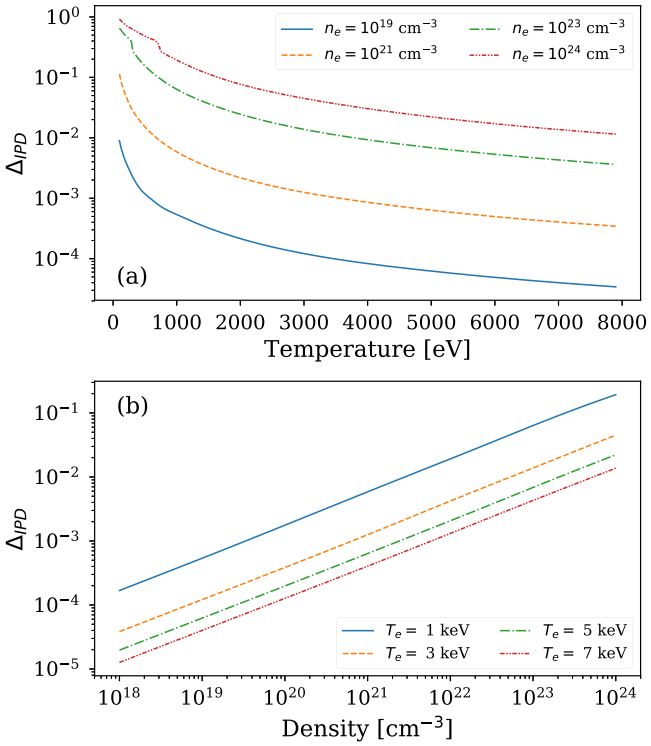

FIG. 3. (a) Relative change in the NEEC rate due to IPD as a function of electron temperature for $n_e = 10^{19}$ cm^{-3} (blue solid curve), $n_e = 10^{21}$ cm^{-3} (orange dashed curve), $n_e = 10^{23}$ cm^{-3} (green dash-dotted curve), and $n_e = 10^{24}$ cm^{-3} (red dash–double-dotted curve). (b) The Δ_{IPD} as a function of electron density for $T_e = 1$ keV (blue solid curve), 3 keV (orange dashed curve), 5 keV (green dash-dotted curve), and 7 keV (red dash–double-dotted curve).

is presented as a function of T_e and n_e. The notation $\lambda^{\mathrm{IPD}}_{\mathrm{NEEC}}$ stands for the rate for which the plasma-induced potential lowering has been taken into account.

As seen from Fig. 3, the IPD leads to a decrease in the NEEC rate for all considered temperature and density values. The relative change becomes however relevant only for low temperatures and high densities. For instance, for $n_e \leqslant 10^{19}$ cm^{-3} or $T_e \geqslant 3$ keV, Δ_{IPD} stays below 1% for the entire temperature or density range, respectively. Only for the extreme case of temperatures below 300 eV and densities higher than 10^{22} cm^{-3}, Δ_{IPD} reaches values of 10% and above, which is nevertheless still within the expected accuracy of our model. Deviations of these relative values when employing IPD models [58–60] other than the one of Stewart and Pyatt also do not lead to a significant change of the NEEC results in the regime of interest.

C. Resonant nuclear photoexcitation

Nuclear excitation in the plasma may occur not only via NEEC but also via other mechanisms. In the considered temperature and density range the resonant nuclear photoexcitation is expected to be the main competing process to NEEC. For this reason we evaluated the photoexcitation rate in the plasma for two scenarios: (i) considering a blackbody radiation spectrum and (ii) considering a photon distribution originating from

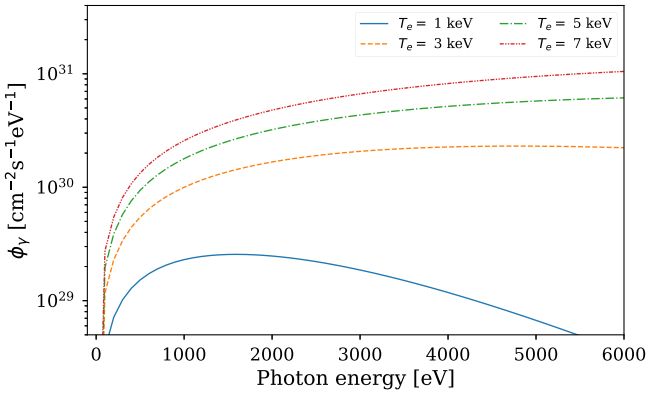

FIG. 4. Blackbody photon flux $\phi^{\mathrm{TDE}}_\gamma$ as a function of photon energy for temperatures $T_e = 1$ keV (blue solid curve), $T_e = 3$ keV (orange dashed curve), $T_e = 5$ keV (green dash-dotted curve), and $T_e = 7$ keV (red dash–double-dotted curve).

bremsstrahlung. The theoretical expressions for the calculation have been given in Sec. II C.

The photon flux for TDE conditions (blackbody radiation) is presented in Fig. 4. In contrast to the electron flux, $\phi^{\mathrm{TDE}}_\gamma$ is independent of the electron density and drastically rises with growing temperature T_e. For the ^{93m}Mo isomer triggering especially the flux at 4.85 keV photon energy is interesting. The flux value increases from 7×10^{28} to 9×10^{30} cm^{-2} s^{-1} eV^{-1} by going from $T_e = 1$ keV to $T_e = 7$ keV.

In Fig. 5, the NEEC rate λ_{NEEC} is plotted together with the photoexcitation rates $\lambda^{\mathrm{TDE}}_\gamma$ and λ^{B}_γ for electron densities 10^{19}, 10^{21}, and 10^{23} cm^{-3}. A comparison of the NEEC rate and the nuclear photoexcitation assuming a blackbody radiation spectrum at the given plasma temperature T_e shows that at $n_e = 10^{21}$ cm^{-3} NEEC dominates for $T_e \lesssim 2$ keV and for higher densities $n_e = 10^{22}$ cm^{-3} up to a temperature of 6 keV. We note that while our NEEC values are to be considered as lower limit estimates, the actual photoexcitation in the plasma

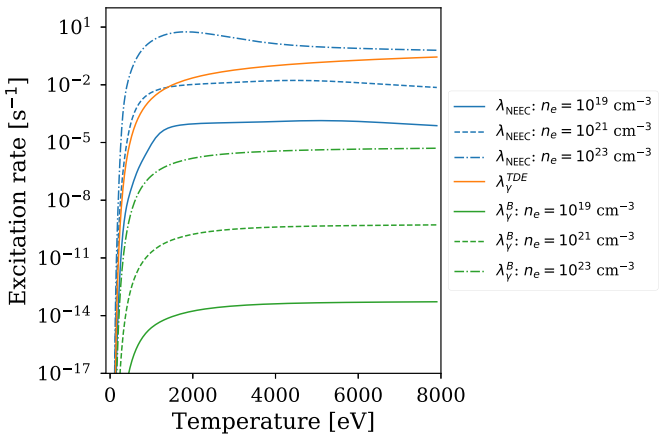

FIG. 5. The NEEC rate λ_{NEEC} [blue (dark gray) curve], photoexcitation rates $\lambda^{\mathrm{TDE}}_\gamma$ [orange (light gray) curve], and λ^{B}_γ [green (medium gray) curve] as functions of electron temperature. For NEEC and for photoexcitation via bremsstrahlung photons, electron densities of 10^{19} cm^{-3} (solid lines), 10^{21} cm^{-3} (dashed lines), and 10^{23} cm^{-3} (dash-dotted lines) have been considered.

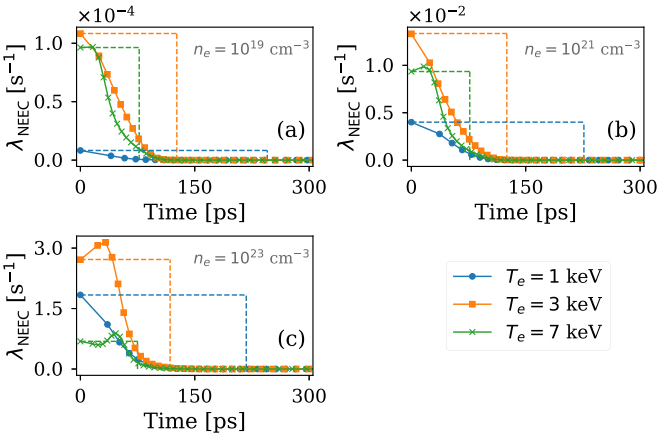

FIG. 6. The NEEC rate λ_{NEEC} as a function of time during the hydrodynamic expansion. We considered initial electron densities (a) 10^{19} cm^{-3}, (b) 10^{21} cm^{-3}, and (c) 10^{23} cm^{-3} and initial temperatures of 1 keV (blue curves with closed circles), 3 keV (orange curves with closed squares), and 7 keV (green curves with crosses). The lifetime estimate is illustrated by the dashed lines.

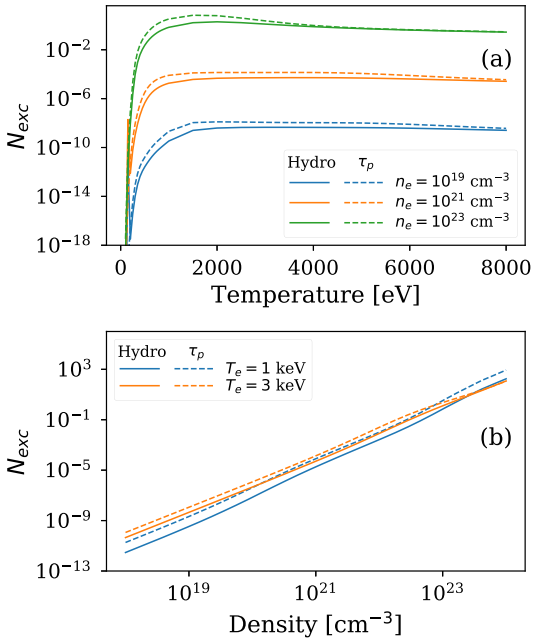

FIG. 7. The NEEC number as a function of (a) temperature and (b) electron density. Results from hydrodynamic expansion (solid curves) are shown in comparison to the lifetime estimate τ_p (dashed curves) for several initial plasma conditions. An initial plasma radius of 40 μm has been considered.

should be lower than the calculated values for a blackbody spectrum in particular at low densities because photons may more easily escape the finite plasma volume. For the high-density $n_e \geqslant 10^{23}$ cm^{-3} parameter regime, NEEC is the dominant nuclear excitation mechanism. The photoexcitation rate λ_γ^B was calculated employing bremsstrahlung cross sections $d\sigma_B(E_e)/dE$ from Ref. [61]. Our results show that the nuclear photoexcitation rate induced by bremsstrahlung photons is always several orders of magnitude lower and can be safely neglected.

D. Plasma expansion: Lifetime approach and hydrodynamic model

So far we have considered the lifetime approach to estimate the total number of excited nuclei via Eq. (14). For a more sophisticated ansatz, we apply the hydrodynamic model for the plasma expansion as introduced in Sec. II D 2 with initial conditions given by the present plasma conditions n_i, T_e, and R_p. In Fig. 6, the time evolution of λ_{NEEC} during the expansion is presented for several initial plasma parameters. As seen from the figure, the NEEC rate decreases over time since the plasma cools down and is diluted in terms of density while expanding. However, for cases where the initial temperature exceeds T_{max} for the given initial density, the NEEC rate first increases, peaking at optimal conditions, and afterward follows the typical decaying pattern, as clearly visible in Fig. 6.

A timescale comparison between the hydrodynamic model and the lifetime approach according to Eq. (17) (illustrated by the dashed lines in Fig. 6) shows that the latter seems to overestimate the NEEC timescale especially for low temperatures. Also, the dependence of the NEEC timescale on T_e is much weaker for the hydrodynamic expansion as determined by Eq. (17). For instance, for $T_e = 1$ and 7 keV at density $n_e = 10^{21}$ cm^{-3}, the lifetime τ_p is given by 226 and 77 ps, respectively. Considering the hydrodynamic expansion, the time integration over λ_{NEEC} roughly converges after 110 and 130 ps, respectively.

Despite this discrepancy in the NEEC timescales between the lifetime and hydrodynamic models, the comparison of the total number of excited nuclei as a function of the plasma conditions in Fig. 7 shows a strikingly similar behavior for the two models. For the calculations, a plasma radius of 40 μm has been used. As a rule, the excitation numbers for the hydrodynamic expansion are slightly smaller than the corresponding ones from the lifetime approach. Furthermore, the highest deviation between the expansion models is at low temperatures and small densities, as already expected from the results in Fig. 6. At a temperature of 1 keV and an electron density of 10^{19} cm^{-3}, the relative difference in the estimated excitation numbers N_{exc} evaluates to 84%, while it is on the order of 5% at the high-temperature ($\geqslant$6 keV) and high-density (10^{23} cm^{-3}) tail.

Overall, the lifetime approach appears to provide reasonable estimates for N_{exc} which deviate from the hydrodynamic model by 40%–80% for low temperatures and small densities. At high T_e and n_e, the predicted excitation numbers almost coincide. As an advantage, the plasma lifetime approach is less computationally expensive and can be applied to a broader range of problems in comparison to the hydrodynamic expansion. For an order of magnitude estimate we therefore proceed to extract the optimal NEEC parameters for optical-laser-generated plasmas with the help of the plasma lifetime τ_p approach.

We note that, following the argument in Ref. [45], we assume for Eq. (21) that all ions have the same velocity dR_t/dt during the expansion. If one assumes the ion velocity at position r to be dr/dt and the velocity scales linearly with the position, the factor 3 in Eq. (22) should be replaced by 5 [62,63]. However, the difference between these two factors

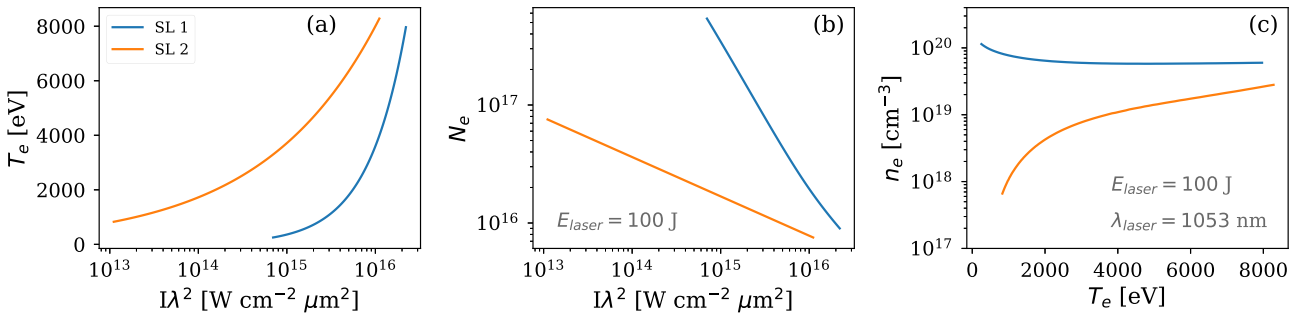

FIG. 8. Accessible plasma parameters for the ponderomotive scaling law [SL1, blue (dark gray) curves] and the short-scale length profile scaling law [SL2, orange (light gray) curves]. The (a) electron temperature and (b) number of free electrons present in the plasma are presented as functions of the laser irradiance $I\lambda^2$. In the calculations of N_e a pulse energy of 100 J is assumed. (c) Corresponding plasma profile $n_e = f(T_e)$ for a laser wavelength of 1053 nm, a pulse energy of 100 J, and intensity ranges $7 \times 10^{14} - 2 \times 10^{16}$ W/cm^2 (SL1) and 10^{13}–10^{16} W/cm^2 (SL2). The results here are independent of τ_{laser}.

should not affect our conclusion on the validity of the lifetime approach for the nuclear excitation calculation. Finally, the expansion with uniform density adopted above is a rather simplified model, but it provides good estimates of the cluster expansion characteristics. For a more accurate model, which is however beyond the scope of the present work, we refer the interested reader to Ref. [64].

IV. LASER PLASMAS

In the following, we proceed to determine how the optimal NEEC parameter region in the temperature-density landscape may be accessed by a short laser pulse. We discern in our treatment two cases, namely, the low- and high-density plasmas, and refine accordingly our plasma model.

A. Low density

First, we consider the case of a low-density (underdense) plasma, which can be generated via the interaction of a strong optical laser with a thin target. The plasma generation process typically evolves in two steps [49]: (i) a preplasma is formed by the prepulse of the laser and (ii) this preplasma is subsequently heated by the main laser pulse potentially up to keV electron energies.

We model the plasma following the approach presented in Sec. II D 3 with the help of so-called scaling laws which provide a unique relation between laser parameters and plasma conditions. We employ two scaling law models: the sharp-edge scaling law (ponderomotive scaling law) in Eq. (24), further denoted by SL1, and the short-scale length profile scaling law in Eq. (25), referred to in the following as SL2.

1. Results of scaling laws

In Figs. 8(a) and 8(b) the electron temperature T_e and the number of free electrons N_e in the plasma are shown as functions of the laser irradiance $I\lambda^2$, respectively, for both scaling laws SL1 and SL2. The considered range of irradiances has been chosen such that the expected electron temperatures span from approximately 300 eV to 8 keV.

The scaling laws SL1 and SL2 should be valid for collisionless heating in the intermediate irradiance regime $I\lambda^2 \sim 10^{16}$W cm^{-2} μm^2 [53]. In particular, SL1 covers the entire parameter regime presented in Fig. 8, while SL2 exceeds its validity domain for the low-temperature case. For the sake of comparison, in the following we compare SL1 and SL2 throughout the entire parameter regime of interest. However, we should keep in mind that at low temperatures (lower than ∼1 keV) we enter an intensity regime lower than the lower limit for SL2 ($I\lambda^2 \sim 10^{14}$W cm^{-2} μm^2) [53,54], in which the collisional heating may be the dominating heating mechanism.

In order to estimate the number of free electrons in the laser-heated plasma the laser absorption coefficient f occurring in Eq. (26) needs to be fixed. In Refs. [65,66] experimental data on the absorption of short laser pulses in the ultrarelativistic regime are presented. A Ti:sapphire laser with 150-fs pulses at 800 nm and an energy up to 20 J was used to heat Al foils (thickness ∼1.5–100 μm) and Si plates (thickness ∼400 μm). The measured laser absorption shows no significant dependence on the target thickness and the material. Moreover, in consistency with previous experiments at lower intensities [66], it could be shown that the absorption mechanisms change from collision dominated to collisionless by exceeding an intensity of around 10^{17} W/cm^2. The experimental results show good agreement with a theoretical calculation based on a Vlasov-Fokker-Planck code. We therefore adopt a universal absorption coefficient $f = f(I\lambda^2)$ as a function of laser irradiance to estimate the absorbed laser energy by performing a cubic interpolation to theoretical results based on a Vlasov-Fokker-Planck code presented in Ref. [65]. A more detailed discussion on the laser absorption coefficient and its impact on the NEEC rates is given in Sec. IV A 2.

As can be seen from Fig. 8, SL2 predicts higher temperatures for a given laser intensity I_{laser}. However, since the number of free electrons is inversely proportional to the electron temperature [see Eq. (26)], the resulting density for SL2 is expected to be smaller in comparison to SL1. For a wavelength of $\lambda_{\text{laser}} = 1053$ nm typical for Nd:glass lasers and a pulse energy of 100 J, the corresponding temperature-density profiles for SL1 and SL2 are presented in Fig. 8(c). With the considered intensity range between 7×10^{14} and 2×10^{16} W/cm^2 for SL1, the absorption fraction f lies between 0.1 and 0.2, leading to electron densities on the order of 10^{20} cm^{-3}. The extension of the low-intensity tail for SL2 (10^{13}–10^{16} W/cm^2) results in slightly higher absorption coefficients up to 30%. However, the electron densities are smaller in this case since

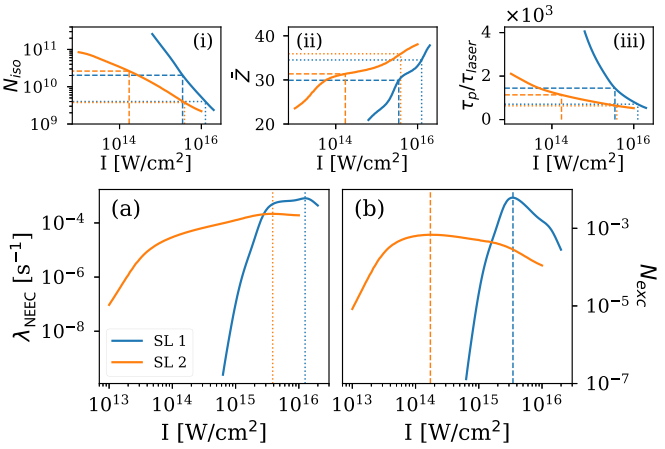

FIG. 9. (a) The NEEC rate λ_{NEEC} and (b) the total excitation number N_{exc} per laser pulse as functions of laser intensity for the ponderomotive scaling law [SL1, blue (dark gray) curves] and the short-scale length profile scaling law [SL2, orange (light gray) curves]. Shown on top are (i) the number of isomers present in the plasma, (ii) the average charge state $\bar{Z}$, and (iii) the plasma lifetime. See the text for further explanations.

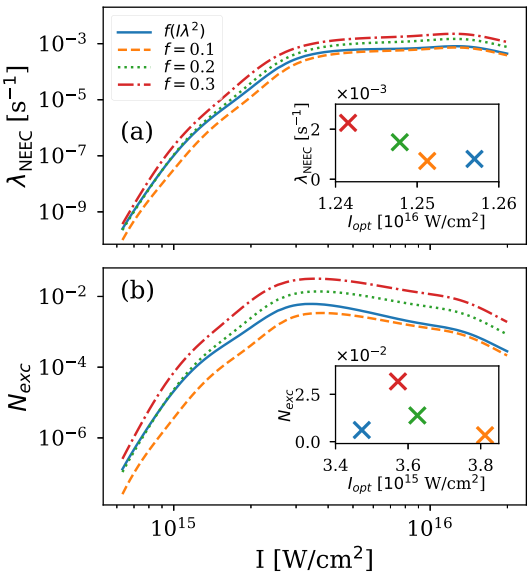

FIG. 10. Impact of the laser absorption f on NEEC results considering SL1 for (a) λ_{NEEC} and (b) N_{exc} as functions of I_{laser} for $f = f(I\lambda^2)$ (blue solid line), $f = 0.1$ (orange dashed line), $f = 0.2$ (green dotted line), and $f = 0.3$ (red dash-dotted line). The inset presents the optimal laser intensities for NEEC for the different f values. See the text for further explanations.

the average electron temperature is higher for a fixed plasma volume V_p.

Numerical results for λ_{NEEC} and for the total excitation number N_{exc} per laser pulse are presented in Fig. 9 as functions of the laser intensity. The plasma expansion time is estimated by using the lifetime approach with the smallest length scale out of R_{focal} and d_p [see Eq. (28)] for a lower-limit estimate of the NEEC. We consider a pulse energy of 100 J, wavelength of 1053 nm, and laser pulse duration values of 500 fs. Apart from λ_{NEEC} and N_{exc}, the number of isomers N_{iso} present in the plasma, the average charge state $\bar{Z}$, and the plasma lifetime τ_p in units of τ_{laser} are shown as functions of the laser intensity.

Analogous to the discrepancy between T_{max} for the NEEC rate and total excitation number, also here the optimal laser intensities I_{opt} at which λ_{NEEC} and N_{exc}, respectively, are maximal do not coincide. For the assumed laser parameters, λ_{NEEC} is maximized by $I_{\mathrm{opt}} = 1.26 \times 10^{16}$ W/cm^2 at a temperature of 5 keV and a density of 5.8×10^{19} cm^{-3} in the case of SL1. In contrast, the optimal intensity for N_{exc} per laser pulse is 3.5×10^{15} W/cm^2. The electron temperature and density achieved at this intensity are 1.4 keV and 7.0×10^{19} cm^{-3}, respectively, leading to a charge state distribution with $\bar{Z} \sim 30$ where capture channels into the M shell still dominate the L-shell contribution. The optimal values for SL2 lie at smaller intensities, 3.9×10^{15} and 1.72×10^{14} W/cm^2 for λ_{NEEC} and N_{exc}, respectively, where plasma conditions $T_e = 6$ keV and $n_e = 3.8 \times 10^{19}$ cm^{-3}, and $T_e = 2.1$ keV and $n_e = 4.7 \times 10^{18}$ cm^{-3}, respectively, are prevailing.

In general, Fig. 9 shows that the total number of excited isomers is maximal at plasma conditions with lower average charge state $\bar{Z}$ but longer plasma lifetime and larger plasma volume in comparison to the optimal conditions for the NEEC rate. The effect of the larger plasma volume can be seen for the number of isomers present in the plasma [Fig. 9(i)], which is given by approximatively 2×10^{10} isomers at I_{opt} for N_{exc}. The proportionality of N_{iso} with respect to the laser irradiance $I\lambda^2$ is given by the relation

$$N_{\mathrm{iso}} \propto \bar{Z} N_e \propto \begin{cases} \bar{Z} f(I\lambda^2)/(I\lambda^2) & \text{for SL1} \\ \bar{Z} f(I\lambda^2)/(I\lambda^2)^{1/3} & \text{for SL2,} \end{cases} \tag{34}$$

where $\bar{Z}$ is itself a function of laser intensity and wavelength for fixed pulse energy E_{pulse}.

2. *Laser absorption*

Since the laser absorption fraction f can be treated as a free parameter in the scaling laws SL1 and SL2, we study the effect of different f values for the NEEC rate in the plasma and the corresponding nuclear excitation. We have performed calculations with constant absorption fractions of 10%, 20%, and 30% considering a pulse energy of 100 J, a laser wavelength of 1053 nm, and a pulse duration of 500 fs. The results, together with a comparison with the laser absorption model $f(I\lambda^2)$, are shown in Fig. 10 for SL1 and Fig. 11 for SL2.

As can be seen from these two figures, the NEEC rate and the total excitation number increase with increasing absorption coefficient f since higher densities are reached. Moreover, the optimal laser intensities depend on the laser absorption, as illustrated in the corresponding insets of the graphs. While the change of I_{opt} due to f is smaller than 10% and hence negligible in terms of the expected accuracy of our model for SL1, the intensity- and wavelength-dependent absorption coefficient f has a much stronger effect on the predictions of SL2 in comparison to a constant absorption fraction. With constant f the optimal intensity for N_{exc} is at approximately 2.5×10^{15} W/cm^2, in comparison to 1.7×10^{14} W/cm^2 with $f(I\lambda^2)$. Note that I_{opt} for λ_{NEEC} is not shown in Fig. 11 since

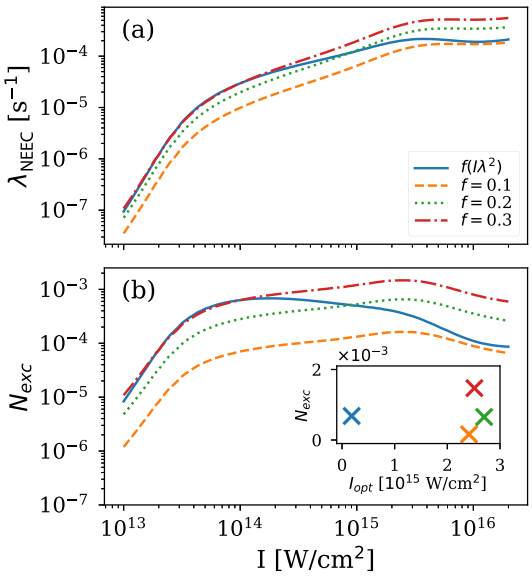

FIG. 11. Impact of the laser absorption f on NEEC results considering SL2. The notation is analogous to that in Fig. 10.

the rate keeps increasing for higher intensities way out of the validity range for the applied scaling law model SL2.

3. Dependence on laser parameters

In this section, we analyze the functional behavior of the NEEC on the laser parameters I_{laser}, λ_{laser}, τ_{laser}, and E_{pulse}. For this analysis we restrict ourselves to the steep density gradients scenario which is best described by SL1 using the universal absorption coefficient $f(I\lambda^2)$. In Fig. 12(a) we present the total number of excited isomers N_{exc} as a function of laser intensity and wavelength for a fixed laser pulse duration of 500 fs and pulse energy of 100 J. It can be seen that the highest excitation numbers can be found for small wavelengths at the corresponding optimal intensity I_{opt} illustrated by the red crosses for given λ_{laser}. The optimal intensity values are increasing with decreasing laser wavelength. We recall that smaller wavelengths lead to smaller electron densities, which require a higher temperature to maximize the NEEC (cf. Fig. 2).

However, typically the wavelength is a parameter determined by the fundamental laser design (i.e., 1053 nm in the case of Nd:glass lasers or 800 nm for Ti:sapphire lasers) and can only be changed by considering higher harmonics. Therefore, it is worth further investigation of the behavior of N_{exc} in terms of variable laser intensity and pulse energy for a given wavelength of, for instance, 1053 nm and pulse duration of 500 fs. Numerical results are shown in Fig. 12(b). As can be expected already from the direct relation between the number of free electrons in the plasma and E_{pulse} [compare Eq. (26)], the NEEC is higher for higher pulse energies. The optimal laser intensity for given E_{pulse} [represented by the red crosses in Fig. 12(b)] is constant over the considered energy range.

For $d_p < R_{\text{focal}}$ (the case for the parameters of Figs. 9–12) the plasma lifetime is determined by d_p and in turn by τ_{pulse}. In order to evaluate the influence of τ_{pulse} on the NEEC process, Fig. 13 shows N_{exc} at the optimal intensity I_{opt} as a function of the pulse duration. For the calculations we considered again

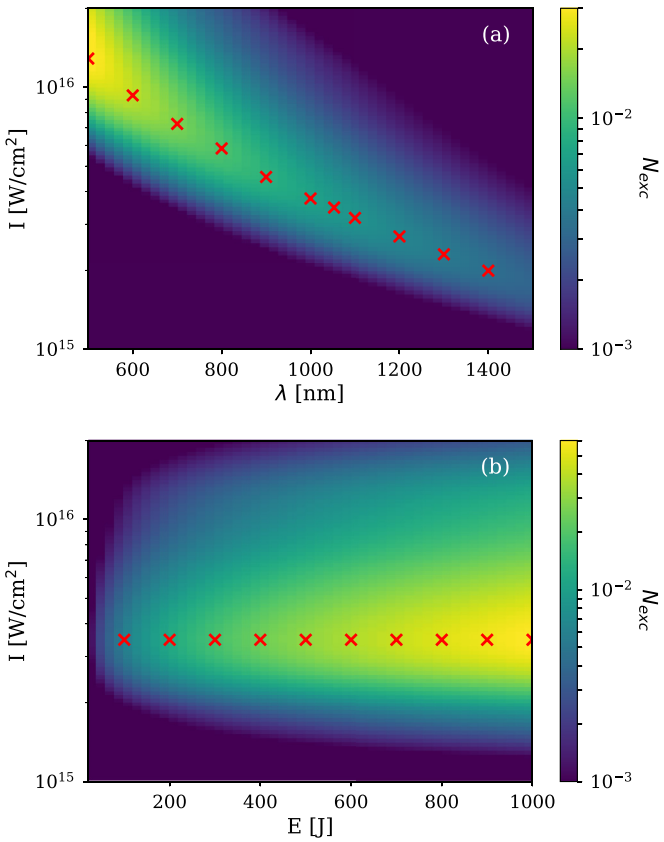

FIG. 12. Total number of excited isomers as a function of laser parameters: (a) $N_{\text{exc}}(I,\lambda)$ for fixed $E_{\text{pulse}} = 100$ J and (b) $N_{\text{exc}}(I,E)$ for fixed $\lambda_{\text{laser}} = 1053$ nm. The pulse duration is assumed to be $\tau_{\text{laser}} = 500$ fs.

a fixed pulse energy of 100 J and a wavelength of 1053 nm. As seen from the figure, the NEEC becomes stronger with increasing laser pulse duration τ_{pulse}, reaching its maximum at 2.2 ps, the value where $d_p = R_{\text{focal}}$. According to our model,

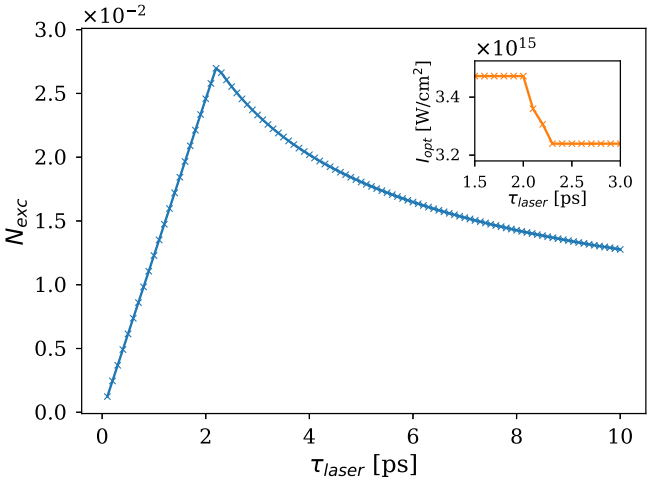

FIG. 13. Total excitation number N_{exc} at optimal intensity as a function of τ_{laser}. The inset shows $I_{\text{opt}}(\tau_{\text{laser}})$ close to the region where N_{exc} is maximized. We considered a pulse energy of 100 J and laser wavelength of 1053 nm.

this condition is satisfied for

$$\tau_{\text{laser}} = \left(\frac{E_{\text{laser}}}{c^2 \pi I_{\text{laser}}} \right)^{1/3}. \tag{35}$$

For even longer pulse durations we need to use R_{focal} in our model to determine the plasma lifetime [see Eq. (28)]. We then notice a decrease of N_{exc} as for a given laser pulse energy, longer τ_{pulse} values require smaller focal radii to obtain the same intensity and in turn shorter plasma lifetime. The optimal intensity shifts slightly to smaller values by going from the parameter region where $d_p < R_{\text{focal}}$ to parameters with $d_p > R_{\text{focal}}$ (see the inset of Fig. 13).

We note that for short-pulse lasers, the plasma lifetime is constrained by the plasma thickness, which depends on the pulse duration and optimally should have a size similar to the other two dimensions encompassed by the focal spot. We have not considered here long, nanosecond laser pulses, which lead to a complex plasma evolution which is difficult to model. While short laser pulses limit the plasma lifetime, long, nanosecond laser pulses in turn come with a small focal spot to obtain the necessary laser intensities. Effectively, the nuclear excitation should be similar in magnitude at a given pulse energy for both short-pulse and nanosecond-pulse lasers.

4. High-power laser facilities

In this section, we evaluate the optimal laser intensity I_{opt} and the expected maximal NEEC N_{exc} for realistic parameters of high-power optical lasers which are available currently or are under construction. Results for the ELI beamlines L4 [67], ELI NP [68,69], PETAL [70], LULI [71], VULCAN [72], and PHELIX [73] lasers are presented in Table I.

For all considered cases, the excitation N_{exc} per laser pulse is orders of magnitude larger than the one in the XFEL-generated cold plasma [24,25]. We note that in the analysis in Refs. [24,25], a $B(E2)$ value of 1 W.u. and an isomer fraction of $\sim 1.8 \times 10^{-7}$ were used. For the comparison presented here, we have recalculated the XFEL excitation number using $B(E2) = 3.5$ W.u. and the isomer fraction ($\sim 10^{-5}$) considered for the present work yielding the result $N_{\text{exc}} \sim 10^{-6}$ for a $T_e = 350$ eV plasma. Moreover, the largest value of 2.2 excitations per pulse should be reached with the PETAL laser, which provides both high laser power and longer pulse duration τ_{pulse}. Table I and Figs. 12 and 13 show that a balance between the laser power and laser pulse duration is beneficial for the excitation number. Note that the values presented here slightly differ from the values provided in Ref. [28], since we have taken into account an additional data point for the fitting of the universal absorption coefficient f to extend the model to smaller irradiances $I\lambda^2$.

B. High density

We now turn to the case of high electron densities, which promises the strongest nuclear excitation according to Fig. 2. Experiments and simulations have shown that it is possible to isochorically heat targets at solid-state density to temperatures of a few hundred eV or even a few keV [38,74,75]. Since in this regime the heating of the target is mainly conducted by secondary particles, i.e., hot electrons generated in the laser-target interaction, a more sophisticated model compared to the low-density case is necessary.

1. PIC simulation

The solid-state isomer target is practically a niobium foil with a 10^{-5} fraction of embedded ^{93m}Mo isomers. We have performed a one-dimensional PIC simulation of a Nb solid target with 1 μm thickness and a Nb density of $n_{\text{Nb}} = 5.5 \times 10^{22}$ cm^{-3} interacting with a high-power laser using the EPOCH code [76]. The isomer fraction is small enough to be neglected here in the determination of the plasma conditions. The laser has a Gaussian profile in time with peak intensity $I = 10^{18}$ W/cm^2, laser duration $\tau_{\text{pulse}} = 500$ fs, and laser wavelength $\lambda = 800$ nm. At the boundary of the simulation box where the laser is introduced, the laser reaches the peak intensity at time $t = 500$ fs. A linear preplasma with a thickness of 0.5 μm is considered in front of the solid target. The simulation box is 4 μm in length and the solid target is placed at the center of the simulation box. Ionization is not included explicitly in the simulation; as a representative order for the electron density, we set the charge state to 10.

To include the effect of atomic ionization and recombination events, we averaged the raw data for electron temperature T_e and ion density n_i from the PIC simulation over 10-nm intervals and used these values as input for the radiative-collisional model implemented in FLYCHK [48] to obtain charge state distributions and (corrected) electron densities. The electron density and temperature values are shown in the bottom and middle panels of Fig. 14 for a number of time instants between 1.5 and 3.5 ps as a function of the target penetration depth x together with first-order polynomial and third-order exponential fits, respectively. We note that due to ionization effects the real temperature is expected to be different from the one obtained in the PIC simulation. We use the latter only as a first approximation.

2. NEEC excitation

For the high-density region, we evaluate the NEEC rate as a function of target depth x and time t by inserting the PIC-simulation results for T_e and the corrected n_e values into

TABLE I. Laser parameters and maximal N_{exc} achieved at the optimal laser intensity $I_{\text{opt}} = 3.4 \times 10^{15}$ W/cm^2 for ELI beamlines L4 [67], PETAL [70], LULI [71], VULCAN [72], and PHELIX [73] and $I_{\text{opt}} = 5.7 \times 10^{15}$ W/cm^2 for ELI NP [68,69] lasers.

Parameter	ELI beamlines	ELI NP	PETAL	LULI	VULCAN	PHELIX
E_{pulse} (J)	1500	250	3500	100	500	200
τ_{pulse} (fs)	150	25	5000	1000	500	500
λ (nm)	1053	800	1053	1053	1053	1053
N_{exc}	2.8×10^{-2}	1.4×10^{-3}	2.2	1.2×10^{-2}	3.1×10^{-2}	1.2×10^{-2}

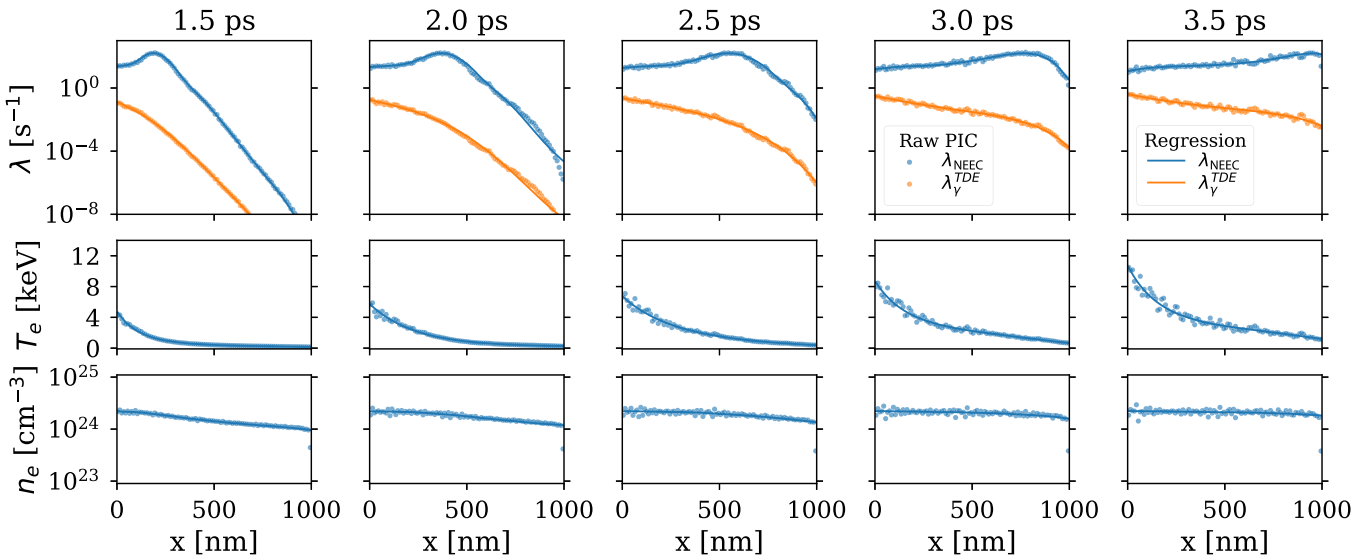

FIG. 14. The top row shows the nuclear excitation rate λ, the middle row the plasma temperature T_e, and the bottom row the electron density n_e based on the PIC simulation as functions of target depth x at time instants 1.5, 2.0, 2.5, 3.0, and 3.5 ps. The NEEC rate λ_{NEEC} [blue (dark gray) curve] is shown in the top-row graphs together with the photoexcitation rate $\lambda_\gamma^{\mathrm{TDE}}$ [orange (light gray) curve]. The laser has peak intensity $I = 10^{18}$ W/cm^2 and wavelength $\lambda = 800$ nm. The raw data averaged over 10-nm intervals are presented together with a linear polynomial and a third-order exponential fit for n_e and T_e, respectively. The raw result of λ_{NEEC} and regression curves for λ_{NEEC} calculated with the fitted n_e and T_e functions are shown in the top-row graphs.

Eqs. (1) and (2). The plasma is assumed to be homogeneous only in the plane perpendicular to the x direction over the region of A_{focal}. We consider a laser pulse energy of 100 J, which leads, for the pulse duration and laser intensity adopted in the PIC simulation, to a focal spot area of approximatively 2×10^{-4} cm^2. Results for λ_{NEEC} and $\lambda_\gamma^{\mathrm{TDE}}$ are presented as a function of x for five time points between $t = 1.5$ and 3.5 ps in the top panel of Fig. 14. The NEEC rate is maximized at depths x where optimal plasma conditions are prevailing. The peak propagates through the target and disappears at around 4 ps as the target heating leads afterward to temperatures exceeding the optimal value for NEEC. A detailed analysis of data sampled from 1 to 4 ps in 100-fs steps shows that the integrated NEEC rate reaches its maximum at 3.1 ps and drops roughly to half its value at 4 ps. Due to the high electron density, λ_{NEEC} is much larger than the photoexcitation rate over the entire target.

The total NEEC rate is shown together with its individual L- and M-shell contributions $\lambda_{\mathrm{NEEC}}^L$ and $\lambda_{\mathrm{NEEC}}^M$, respectively, in Fig. 15 at the time instant of 3.1 ps, where the integrated value reaches its maximum. The figure shows that the flat region mainly comes from the capture into the M shell, which is available (almost) over the whole temperature-density landscape. In contrast, the L-shell NEEC orbitals are only accessible in a very limited region in terms of plasma conditions, leading to the peak in λ_{NEEC} at a target depth x where optimal conditions for L-shell NEEC are prevailing.

Using the regression curves for λ_{NEEC} calculated with the fitted n_e and T_e functions, we solve Eq. (7) in a two-step procedure to obtain the total NEEC number N_{exc}. First, for each time instant t the product of the NEEC rate and the isomer density is integrated with respect to x over the entire target thickness d_t and multiplied by the focal spot area A_{focal} to account for the perpendicular directions. Second, the outcomes of the spatial integration are interpolated as a function of time leading to $N_{\mathrm{exc}}(t)$, which is defined as the derivative with respect to time of the number of excited isomers from initial time t_0 (here 1 ps) up to t,

$$N_{\mathrm{exc}}(t) = \int_{V_p} d^3\mathbf{r}\, n_{\mathrm{iso}}(\mathbf{r},t)\lambda_{\mathrm{NEEC}}(T_e,n_e;\mathbf{r},t). \qquad (36)$$

The interpolation for $N_{\mathrm{exc}}(t)$ is then inserted in the time integral in Eq. (7), which is solved numerically.

For $t > 4$ ps, we extrapolate $N_{\mathrm{exc}}(t)$ assuming an exponential functional behavior initially following the slope at 4 ps. The time integration starting from 1 ps converges approximatively after 10 ps, leading to an excitation number of 1.8 isomers per

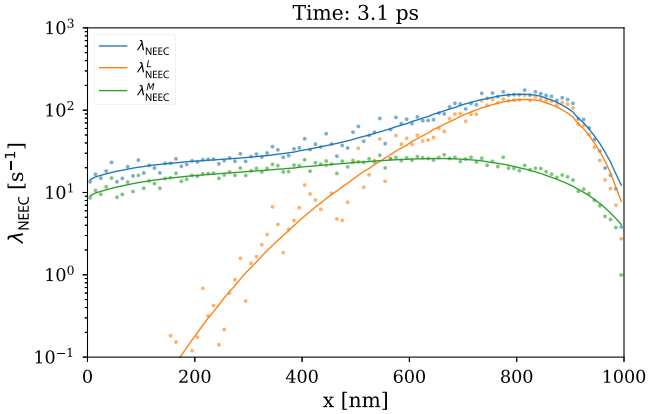

FIG. 15. The NEEC rate λ_{NEEC} and regression curves for λ_{NEEC} calculated with the fitted n_e and T_e functions for the total rate [blue (dark gray)] as well as individual L-shell [orange (light gray)] and M-shell [green (medium gray)] contributions as a function of target depth x.

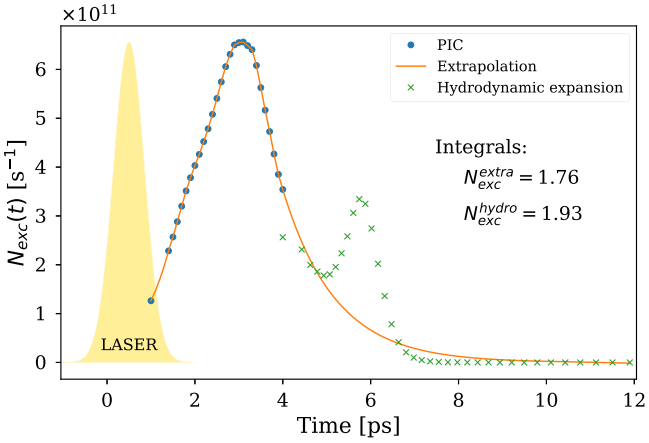

FIG. 16. Time-dependent nuclear excitation number $N_{\mathrm{exc}}(t)$ for PIC results (blue circles). For $t > 4$ ps either an extrapolation (orange curve) or a hydrodynamic expansion (green crosses) is used to estimate N_{exc}. The laser pulse duration is schematically illustrated by the yellow area.

pulse via NEEC, which is almost identical to the best value at low densities obtained with the PETAL parameters and again six orders of magnitude higher than the excitation in the XFEL scenario discussed in Refs. [24,25]. Notable here is that in the high-density case a 100-J laser available at many facilities around the world is competitive with a kJ-laser facility.

3. *Modeling of the plasma expansion*

The extrapolation method described above is equivalent to the assumption that the plasma heating continues after 4 ps. However, since no further energy is placed into the system, the plasma heating should decrease and finally turn into cooling during the plasma expansion. For a cross-check, we consider the plasma expansion to set in directly at 4 ps and use a hydrodynamic model to estimate N_{exc}. We consider the average ion density and electron temperature at 4 ps as input for our hydrodynamic expansion model introduced in Sec. II D 2 assuming homogeneous plasma conditions over the plasma volume $V_p = A_{\mathrm{focal}} d_t$. The results for the excitation number differential in time are shown in Fig. 16 for both the extrapolation and the expansion model.

During the cooling phase, $N_{\mathrm{exc}}(t)$ reaches again a local maximum at the time where $T_e = T_{\max}$ for the given density (see Fig. 16). However, since the density is also strongly decreasing during the expansion, the net effect for the excitation number is small. Our calculations show that the extrapolation method and the hydrodynamic expansion deliver similar results for N_{exc} with a deviation of 10%. Moreover, the values from both methods are in good agreement (within a 20% interval) with a simple lifetime estimate where according to Eq. (17) the plasma exists for additional 2 ps with homogeneous plasma conditions given by the averaged values at $t = 4$ ps.

Note that the PIC simulation has been carried out in the direction with the smallest length scale of the plasma such that our model underestimates the plasma lifetime and only gives a lower limit for the excitation number. Modeling the expansion in the perpendicular direction of the laser incidence with the length scale set by the focal radius, a 10- to 100-fold longer lifetime can be expected to boost N_{exc}.

V. CONCLUSION

Our results show that by a proper choice of target and optical-laser parameters, the plasma conditions can be tailored to optimize nuclear excitation via the NEEC process. For the case of ^{93m}Mo, both low-density and high-density plasmas promise observable depletion of the isomer. The induced excitation is expected to be six orders of magnitude higher than secondary NEEC in an XFEL-produced cold plasma and in turn a factor 10^{11} up to 10^{12} higher than the direct photoexcitation with the XFEL. Allegedly, the absolute number of depleted isomers remains small, mainly due to the fact that the number of isomers in the microscopic plasma volume is small and only a 10^{-10} fraction of them gets depleted.

An excitation number of approximatively two isomers per pulse from our conservative estimate together with laser repetition rates of up to tens of Hz for 100-J pulses reaches the threshold of one isomer depletion per second and should provide a detectable signal. The experimental signature of the nuclear excitation in the plasma would be a γ-ray photon of approximately 1 MeV released in the decay cascade of the triggering level in ^{93}Mo. An evaluation of the plasma blackbody and bremsstrahlung radiation spectra at this photon energy shows that the signal-to-background ratio is very high. An enhancement of the signal could be achieved by employing a combination of optical and x-ray lasers as envisaged for instance at HIBEF [77] at the European XFEL [78]. X-ray-generated inner-shell holes could then provide the optimal capture state in the L-shell orbitals independently from the hot plasma conditions.

[1] T. H. Maiman, Nature (London) **187**, 493 (1960).
[2] A. Di Piazza, C. Müller, K. Z. Hatsagortsyan, and C. H. Keitel, Rev. Mod. Phys. **84**, 1177 (2012).
[3] A. I. Chumakov, A. Q. R. Baron, I. Sergueev, C. Strohm, O. Leupold, Y. Shvyd'ko, G. Smirnov, R. Rüffer, Y. Inubushi, Y. Yabashi, K. Tono, T. Kudo, and T. Ishikawa, Nat. Phys. **14**, 261 (2018).
[4] P. Mulser and D. Bauer, *High Power Laser-Matter Interaction*, Springer Tracts in Modern Physics Vol. 238 (Springer Science + Business Media, Berlin, 2010).
[5] M. R. Harston and J. F. Chemin, Phys. Rev. C **59**, 2462 (1999).
[6] G. Gosselin and P. Morel, Phys. Rev. C **70**, 064603 (2004).
[7] G. Gosselin, V. Méot, and P. Morel, Phys. Rev. C **76**, 044611 (2007).
[8] P. Morel, V. Méot, G. Gosselin, D. Gogny, and W. Younes, Phys. Rev. A **69**, 063414 (2004).
[9] V. Méot, J. Aupiais, P. Morel, G. Gosselin, F. Gobet, J. N. Scheurer, and M. Tarisien, Phys. Rev. C **75**, 064306 (2007).
[10] P. Morel, V. Méot, G. Gosselin, G. Faussurier, and C. Blancard, Phys. Rev. C **81**, 034609 (2010).

[11] M. Comet, G. Gosselin, V. Méot, P. Morel, J.-C. Pain, D. Denis-Petit, F. Gobet, F. Hannachi, M. Tarisien, and M. Versteegen, Phys. Rev. C **92**, 054609 (2015).

[12] K. W. D. Ledingham *et al.*, Phys. Rev. Lett. **84**, 899 (2000).

[13] T. E. Cowan, A. W. Hunt, T. W. Phillips, S. C. Wilks, M. D. Perry, C. Brown, W. Fountain, S. Hatchett, J. Johnson, M. H. Key, T. Parnell, D. M. Pennington, R. A. Snavely, and Y. Takahashi, Phys. Rev. Lett. **84**, 903 (2000).

[14] P. Gibbon, *Short Pulse Laser Interactions with Matter: An Introduction* (Imperial College Press, London, 2005).

[15] K. M. Spohr, M. Shaw, W. Galster, K. W. D. Ledingham, L. Robson, J. M. Yang, P. McKenna, T. McCanny, J. J. Melone, K.-U. Amthor, F. Ewald, B. Liesfeld, H. Schwoerer, and R. Sauerbrey, New J. Phys. **10**, 043037 (2008).

[16] G. Mourou and T. Tajima, Science **331**, 41 (2011).

[17] P. A. Chodash, J. T. Burke, E. B. Norman, S. C. Wilks, R. J. Casperson, S. E. Fisher, K. S. Holliday, J. R. Jeffries, and M. A. Wakeling, Phys. Rev. C **93**, 034610 (2016).

[18] C. J. Cerjan *et al.*, J. Phys. G **45**, 033003 (2018).

[19] A. V. Andreev, R. V. Volkov, V. M. Gordienko, A. M. Dykhne, M. P. Kalashnikov, P. M. Mikheev, P. V. Nikles, A. B. Savel'ev, E. V. Tkalya, R. A. Chalykh, and O. V. Chutko, J. Exp. Theor. Phys. **91**, 1163 (2000).

[20] A. V. Andreev, V. M. Gordienko, and A. B. Savel'ev, Quantum Electron. **31**, 941 (2001).

[21] C. Granja, J. Kuba, A. Haiduk, and O. Renner, Nucl. Phys. A **784**, 1 (2007).

[22] O. Renner, L. Juha, J. Krasa, E. Krousky, M. Pfeifer, A. Velyhan, C. Granja, J. Jakubek, V. Linhart, T. Slavicek, Z. Vykydal, S. Pospisil, J. Kravarik, J. Ullschmied, A. Andreev, T. Kämpfer, I. Uschmann, and E. Förster, Laser Part. Beams **26**, 249 (2008).

[23] F. Gobet, C. Plaisir, F. Hannachi, M. Tarisien, T. Bonnet, M. Versteegen, M. Aléonard, G. Gosselin, V. Méot, and P. Morel, Nucl. Instrum. Methods Phys. Res. Sect. A **653**, 80 (2011).

[24] J. Gunst, Y. A. Litvinov, C. H. Keitel, and A. Pálffy, Phys. Rev. Lett. **112**, 082501 (2014).

[25] J. Gunst, Y. Wu, N. Kumar, C. H. Keitel, and A. Pálffy, Phys. Plasmas **22**, 112706 (2015).

[26] V. I. Goldanskii and V. A. Namiot, Phys. Lett. B **62**, 393 (1976).

[27] A. Pálffy, Contemp. Phys. **51**, 471 (2010).

[28] Y. Wu, J. Gunst, C. H. Keitel, and A. Pálffy, Phys. Rev. Lett. **120**, 052504 (2018).

[29] G. D. Dracoulis, P. M. Walker, and F. G. Kondev, Rep. Prog. Phys. **79**, 076301 (2016).

[30] P. Walker and G. Dracoulis, Nature (London) **399**, 35 (1999).

[31] A. Aprahamian and Y. Sun, Nat. Phys. **1**, 81 (2005).

[32] D. Belic, C. Arlandini, J. Besserer, J. de Boer, J. J. Carroll, J. Enders, T. Hartmann, F. Käppeler, H. Kaiser, U. Kneissl, M. Loewe, H. J. Maier, H. Maser, P. Mohr, P. von Neumann-Cosel, A. Nord, H. H. Pitz, A. Richter, M. Schumann, S. Volz, and A. Zilges, Phys. Rev. Lett. **83**, 5242 (1999).

[33] C. B. Collins, F. Davanloo, M. C. Iosif, R. Dussart, J. M. Hicks, S. A. Karamian, C. A. Ur, I. I. Popescu, V. I. Kirischuk, J. J. Carroll, H. E. Roberts, P. McDaniel, and C. E. Crist, Phys. Rev. Lett. **82**, 695 (1999).

[34] D. Belic *et al.*, Phys. Rev. C **65**, 035801 (2002).

[35] J. J. Carroll, Laser Phys. Lett. **1**, 275 (2004).

[36] A. Pálffy, J. Evers, and C. H. Keitel, Phys. Rev. Lett. **99**, 172502 (2007).

[37] C. J. Chiara, J. J. Carroll, M. P. Carpenter, J. P. Greene, D. J. Hartley, R. V. F. Janssens, G. L. Lane, J. C. Marsh, D. A. Matters, M. Polasik, J. Rzadkiewicz, D. Seweryniak, S. Zhu, S. Bottoni, A. B. Hayes, and S. A. Karamian, Nature (London) **554**, 216 (2018).

[38] Y. Sentoku, A. J. Kemp, R. Presura, M. S. Bakeman, and T. E. Cowan, Phys. Plasmas **14**, 122701 (2007).

[39] L. G. Huang, M. Bussmann, T. Kluge, A. L. Lei, W. Yu, and T. E. Cowan, Phys. Plasmas **20**, 093109 (2013).

[40] J. Oxenius, *Kinetic Theory of Particles and Photons* (Springer, Berlin, 1986).

[41] A. Pálffy, W. Scheid, and Z. Harman, Phys. Rev. A **73**, 012715 (2006).

[42] A. Pálffy, Z. Harman, and W. Scheid, Phys. Rev. A **75**, 012709 (2007).

[43] P. Ring and P. Schuck, *The Nuclear Many-Body Problem* (Springer, New York, 1980).

[44] Experimental Nuclear Reaction Data (EXFOR),2017, http://www-nds.iaea.org/exfor/exfor.htm.

[45] V. P. Krainov and M. B. Smirnov, Phys. Rep. **370**, 237 (2002).

[46] T. Ditmire, T. Donnelly, A. M. Rubenchik, R. W. Falcone, and M. D. Perry, Phys. Rev. A **53**, 3379 (1996).

[47] FLYCHK at IAEA, 2018, https://www-amdis.iaea.org/FLYCHK/.

[48] H.-K. Chung, M. H. Chen, W. L. Morgan, Y. Ralchenko, and R. W. Lee, High Energy Density Phys. **1**, 3 (2005).

[49] J. Fuchs, P. Antici, E. d'Humières, E. Lefebvre, M. Borghesi, E. Brambrink, C. A. Cecchetti, M. Kaluza, V. Malka, M. Manclossi, S. Meyroneinc, P. Mora, J. Schreiber, T. Toncian, H. Pépin, and P. Audebert, Nat. Phys. **2**, 48 (2006).

[50] Y. Wu and A. Pálffy, Astrophys. J. **838**, 55 (2017).

[51] F. Brunel, Phys. Rev. Lett. **59**, 52 (1987).

[52] G. Bonnaud, P. Gibbon, J. Kindel, and E. Williams, Laser Part. Beams **9**, 339 (1991).

[53] P. Gibbon and E. Förster, Plasma Phys. Controlled Fusion **38**, 769 (1996).

[54] P. Gibbon and A. R. Bell, Phys. Rev. Lett. **68**, 1535 (1992).

[55] F. Parpia, C. Fischer, and I. Grant, Comput. Phys. Commun. **94**, 249 (1996).

[56] M. Hasegawa, Y. Sun, S. Tazaki, K. Kaneko, and T. Mizusaki, Phys. Lett. B **696**, 197 (2011).

[57] J. C. Stewart and K. D. Pyatt, Jr., Astrophys. J. **144**, 1203 (1966).

[58] O. Ciricosta *et al.*, Phys. Rev. Lett. **109**, 065002 (2012).

[59] S. X. Hu, Phys. Rev. Lett. **119**, 065001 (2017).

[60] C. Lin, G. Röpke, W.-D. Kraeft, and H. Reinholz, Phys. Rev. E **96**, 013202 (2017).

[61] R. Pratt, H. Tseng, C. Lee, L. Kissel, C. MacCallum, and M. Riley, At. Data Nucl. Data Tables **20**, 175 (1977).

[62] A. Gupta, T. M. Antonsen, and H. M. Milchberg, Phys. Rev. E **70**, 046410 (2004).

[63] P. Hilse, M. Moll, M. Schlanges, and T. Bornath, Laser Phys. **19**, 428 (2009).

[64] X. Gao, A. V. Arefiev, R. C. Korzekwa, X. Wang, B. Shim, and M. C. Downer, J. Appl. Phys. **114**, 034903 (2013).

[65] Y. Ping, R. Shepherd, B. F. Lasinski, M. Tabak, H. Chen, H. K. Chung, K. B. Fournier, S. B. Hansen, A. Kemp, D. A. Liedahl, K. Widmann, S. C. Wilks, W. Rozmus, and M. Sherlock, Phys. Rev. Lett. **100**, 085004 (2008).

[66] D. F. Price, R. M. More, R. S. Walling, G. Guethlein, R. L. Shepherd, R. E. Stewart, and W. E. White, Phys. Rev. Lett. **75**, 252 (1995).

[67] ELI beamlines, L4 beamline,2018, https://www.eli-beams.eu/en/facility/lasers/laser-4-10-pw-2-kj/.
[68] F. Negoita *et al.*, Rom. Rep. Phys. **68**, S37 (2016).
[69] Extreme Light Infrastructure, Nuclear Physics, 2018, http://www.eli-np.ro/.
[70] A. Casner, T. Caillaud, S. Darbon, A. Duval, I. Thfouin, J. P. Jadaud, J. P. LeBreton, C. Reverdin, B. Rosse, R. Rosch, N. Blanchot, B. Villette, R. Wrobel, and J. L. Miquel, High Energy Density Phys. **17**, 2 (2015).
[71] LULI2000 laser system, 2018, https://portail.polytechnique.edu/luli/en/facilities/luli2000/luli2000-laser-system.
[72] Central Laser Facility, Vulcan laser, 2018, https://www.clf.stfc.ac.uk/Pages/Vulcan-laser.aspx.
[73] Petawatt High-Energy Laser for Heavy Ion Experiments (PHELIX), 2018, https://www.gsi.de/en/work/research/appamml/plasma_physicsphelix/phelix.htm.
[74] A. Saemann, K. Eidmann, I. E. Golovkin, R. C. Mancini, E. Andersson, E. Förster, and K. Witte, Phys. Rev. Lett. **82**, 4843 (1999).
[75] P. Audebert, R. Shepherd, K. B. Fournier, O. Peyrusse, D. Price, R. Lee, P. Springer, J.-C. Gauthier, and L. Klein, Phys. Rev. Lett. **89**, 265001 (2002).
[76] T. D. Arber, K. Bennett, C. S. Brady, A. Lawrence-Douglas, M. G. Ramsay, N. J. Sircombe, P. Gillies, R. G. Evans, H. Schmitz, A. R. Bell, and C. P. Ridgers, Plasma Phys. Controlled Fusion **57**, 113001 (2015).
[77] Helmholtz International Beamline for Extreme Fields at the European XFEL, 2018, https://www.hzdr.de/db/Cms?pNid=427&pOid=35325.
[78] European XFEL, 2018, http://www.xfel.eu/.